
This item was submitted to [Loughborough's Research Repository](#) by the author.
Items in Figshare are protected by copyright, with all rights reserved, unless otherwise indicated.

Supplementary information files for "Quantum confinement-induced anti-electrooxidation of metallic nickel electrocatalysts for hydrogen oxidation"

PLEASE CITE THE PUBLISHED VERSION

LICENCE

CC BY 4.0

REPOSITORY RECORD

Zhou, Yuanyuan, Wei Yuan, Mengting Li, Zhenyang Xie, Xiaoyun Song, Yang Yang, Jian Wang, et al. 2024. "Supplementary Information Files for "quantum Confinement-induced Anti-electrooxidation of Metallic Nickel Electrocatalysts for Hydrogen Oxidation"". Loughborough University.
<https://doi.org/10.17028/rd.lboro.28497740.v1>.

Quantum confinement-induced anti-electrooxidation of metallic nickel electrocatalysts for hydrogen oxidation

In the format provided by the
authors and unedited

Supplementary Information

Quantum confinement-induced anti-electrooxidation of metallic nickel electrocatalysts for hydrogen oxidation

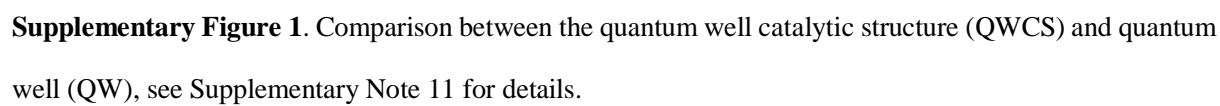
This PDF file includes:

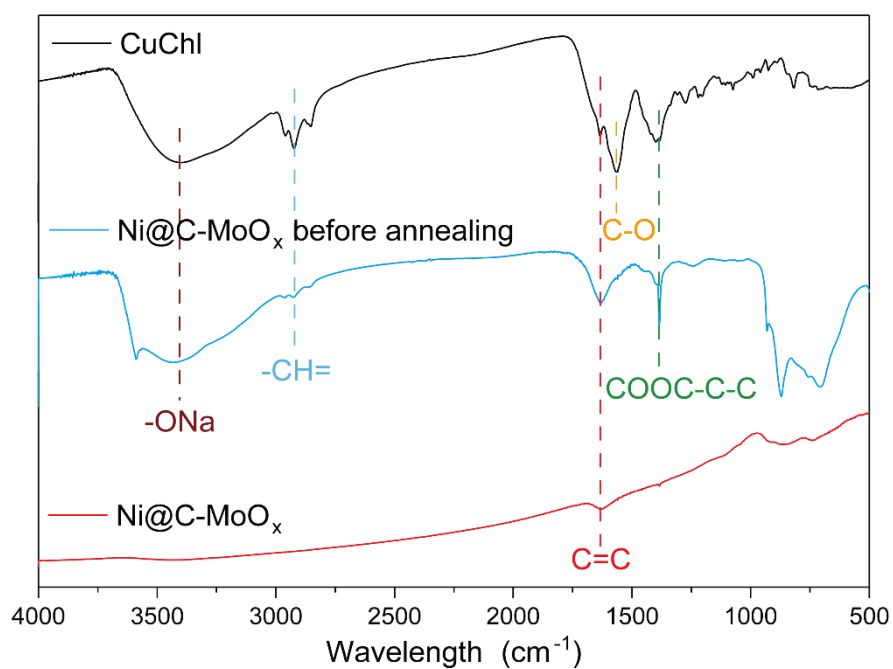
Supplementary Figures 1 to 53

Supplementary Tables 1 to 12

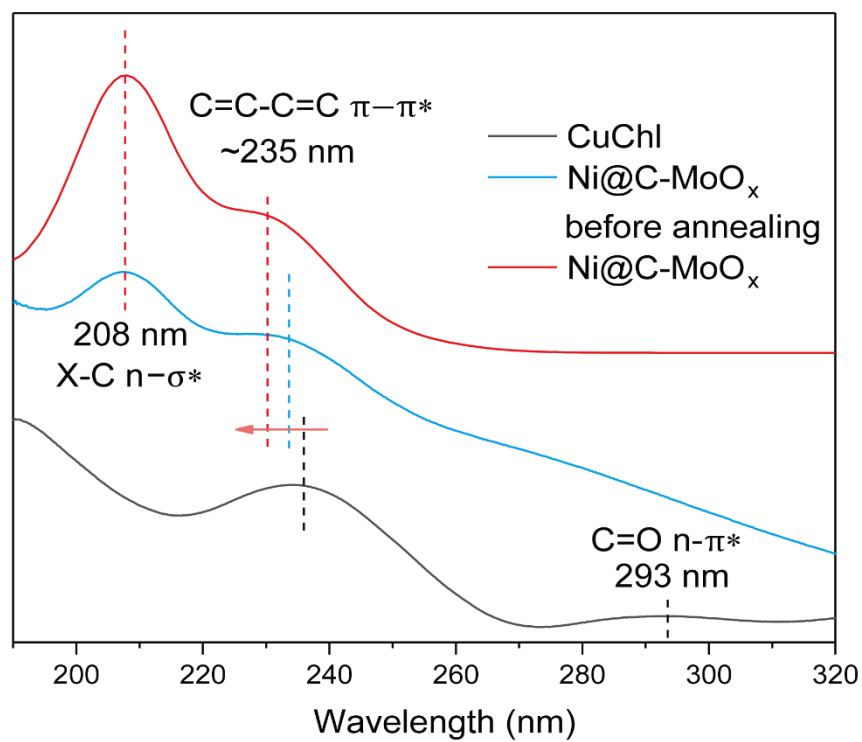
Supplementary Notes 1 to 16

Supplementary References 1 to 7

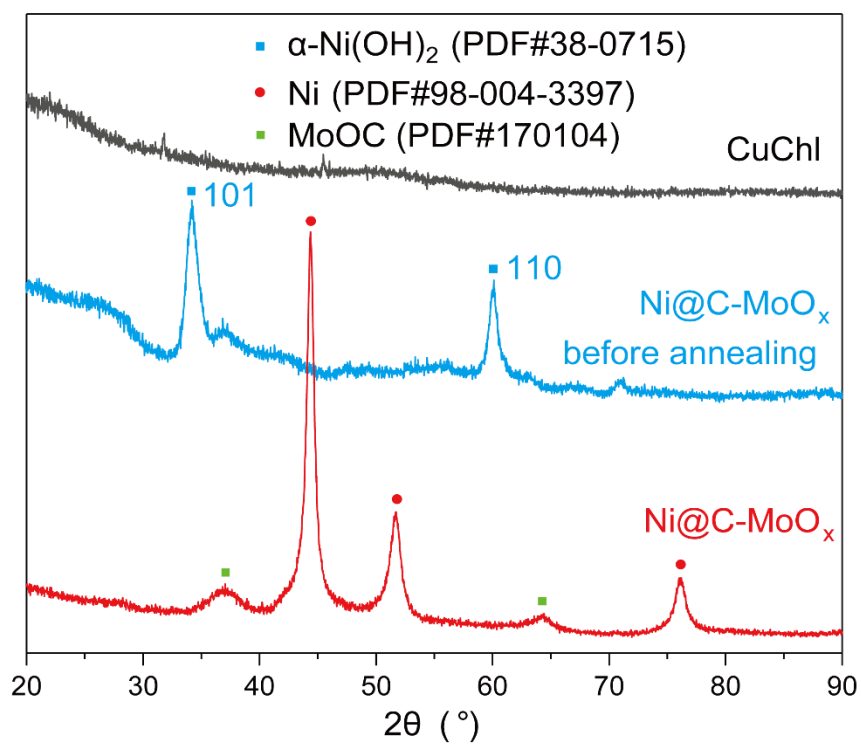




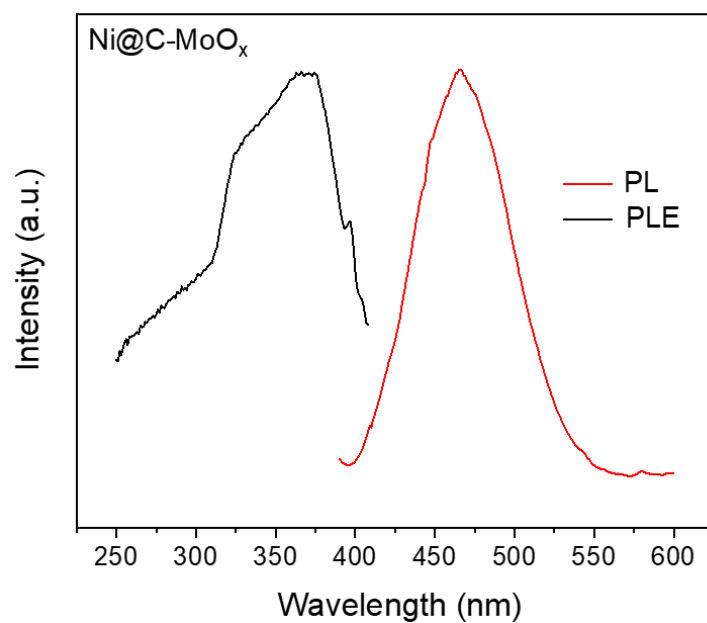
Supplementary Figure 2. FT-IR absorption spectra of Ni@C-MoO_x recorded before and after annealing treatment, also shown here is the spectrum of CuChl for comparison.



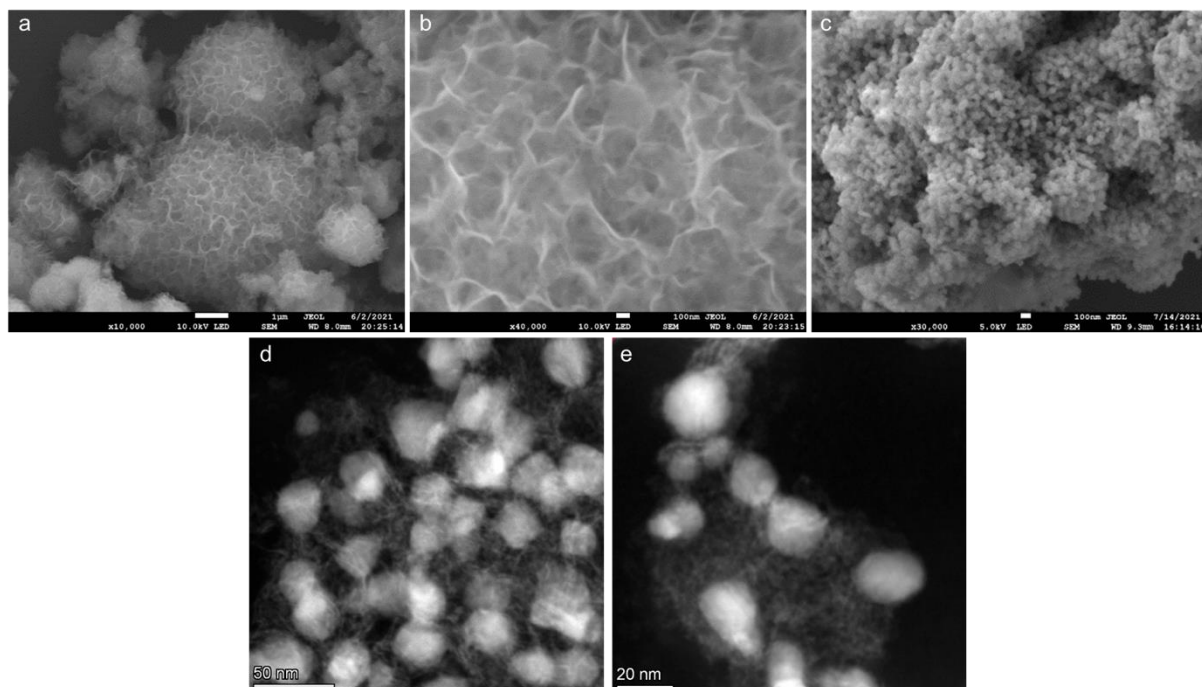
Supplementary Figure 3. UV-vis absorption spectra of Ni@C-MoO_x recorded before (blue) and after (red) annealing treatment, also shown here is the spectrum of CuChl (black) for comparison.



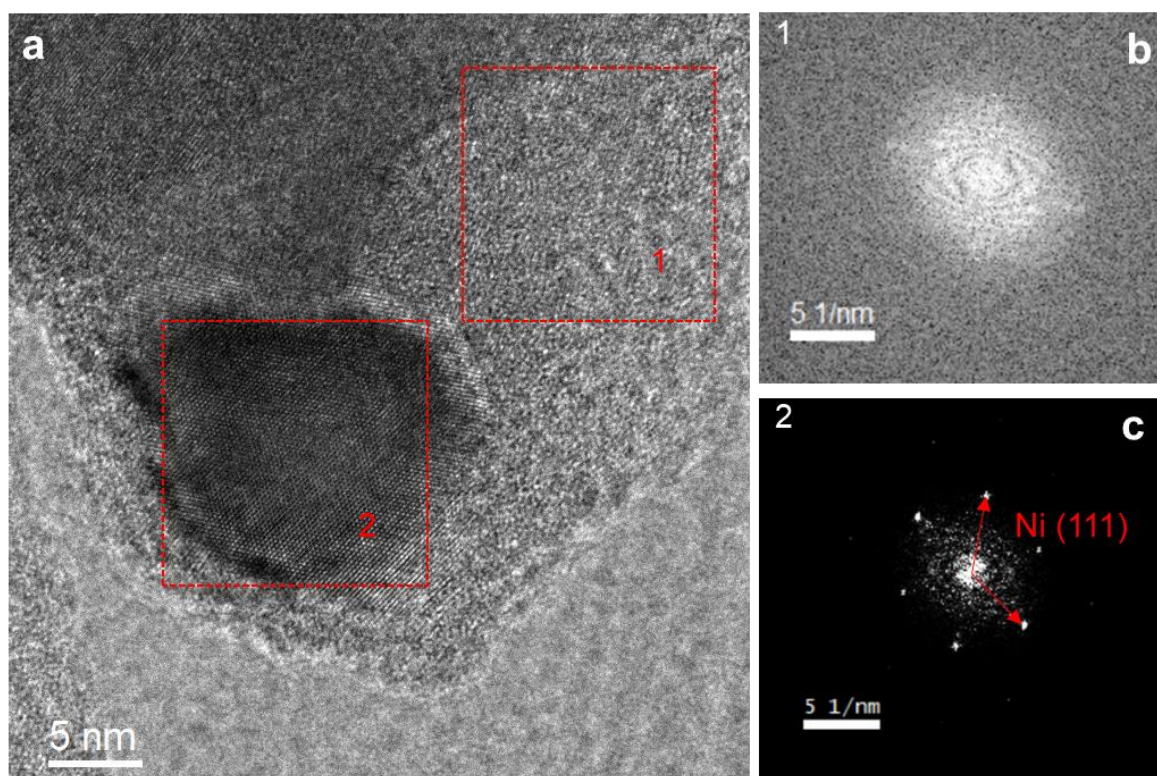
Supplementary Figure 4. XRD patterns of Ni@C-MoO_x recorded before and after annealing treatment, also shown here is the XRD pattern of sodium copper chlorophyllin (CuChl) for comparison.



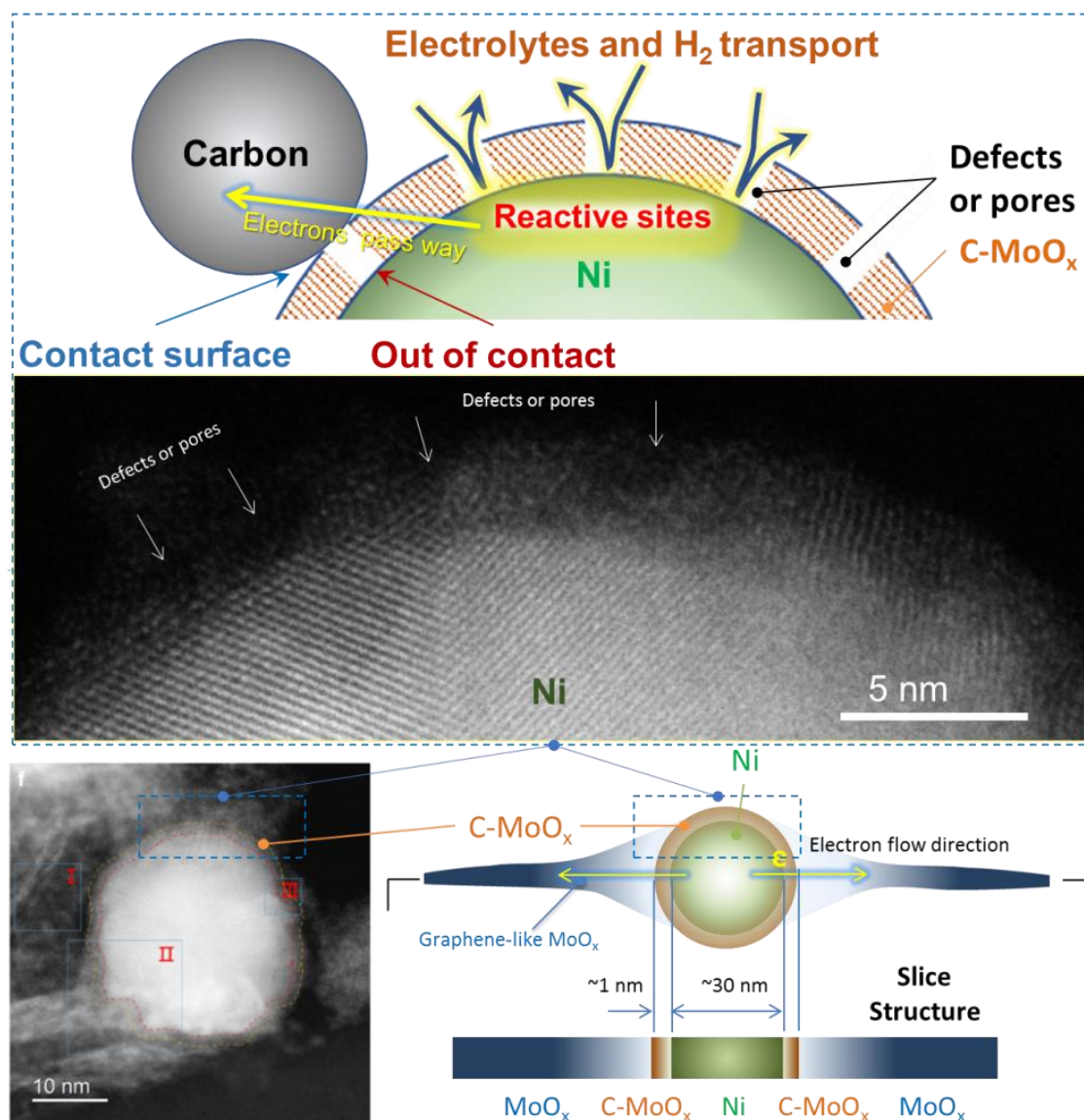
Supplementary Figure 5. Photoluminescence (PL) and Photoluminescence excitation (PLE) spectra of the Ni@C-MoO_x at room temperature. The PL spectrum exhibits a characteristic emission under an excitation wavelength of 390 nm, and the PLE spectrum shows a characteristic excitation with an emission maximum at 463 nm.



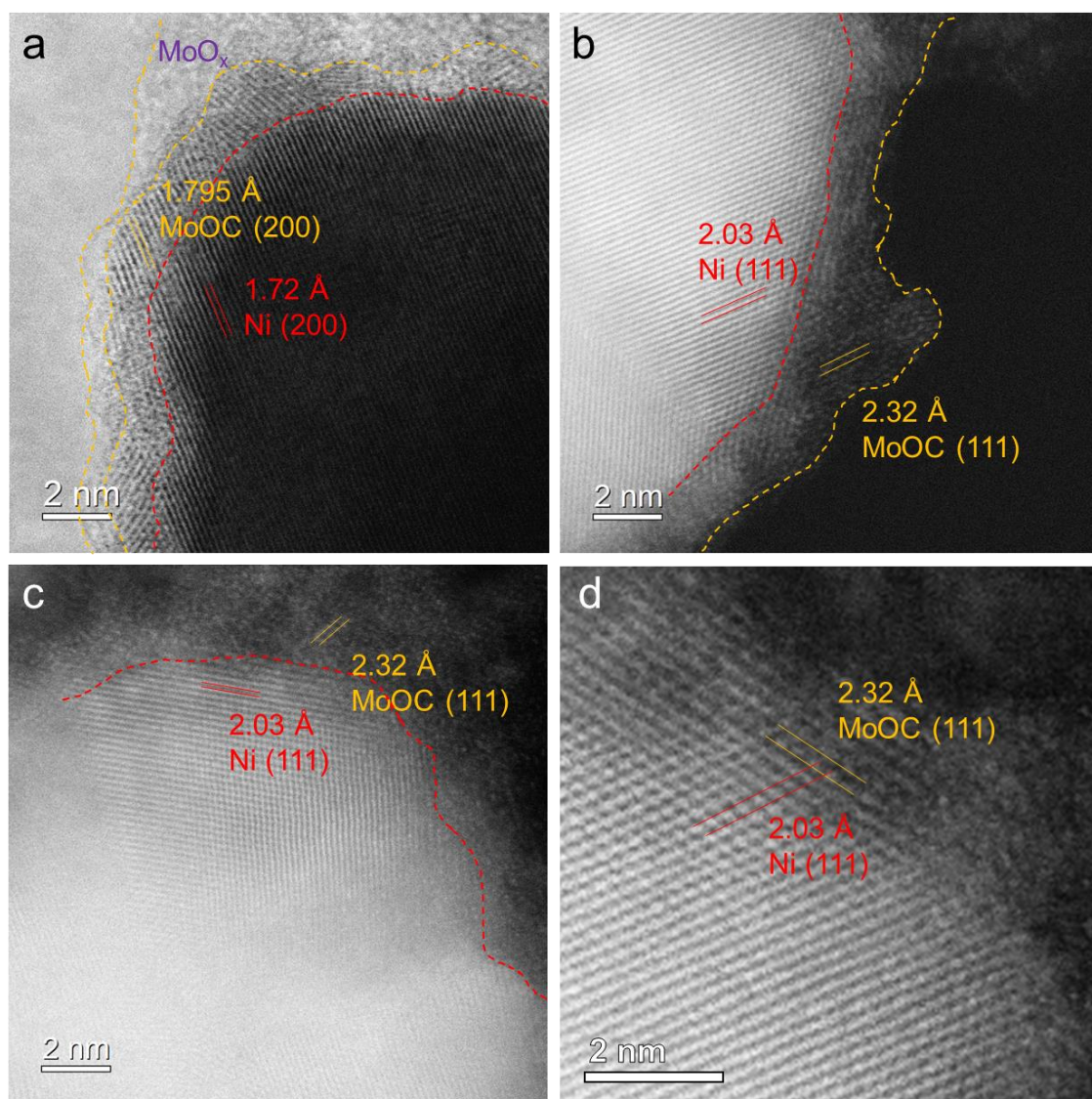
Supplementary Figure 6. SEM images for Ni@C-MoO_x before (a, b) and after (c) annealing. (a) $\times 10000$, 10.0 kV LED, SEM WD 8.0mm; (b) $\times 40000$, 10.0 kV LED, SEM WD 8.0mm; (c) $\times 30000$, 4.0 kV LED, SEM WD 9.3 mm. Scale: 1 μ m (a), 200 nm (b), 200 nm (c). (d, e) TEM images of Ni@C-MoO_x.



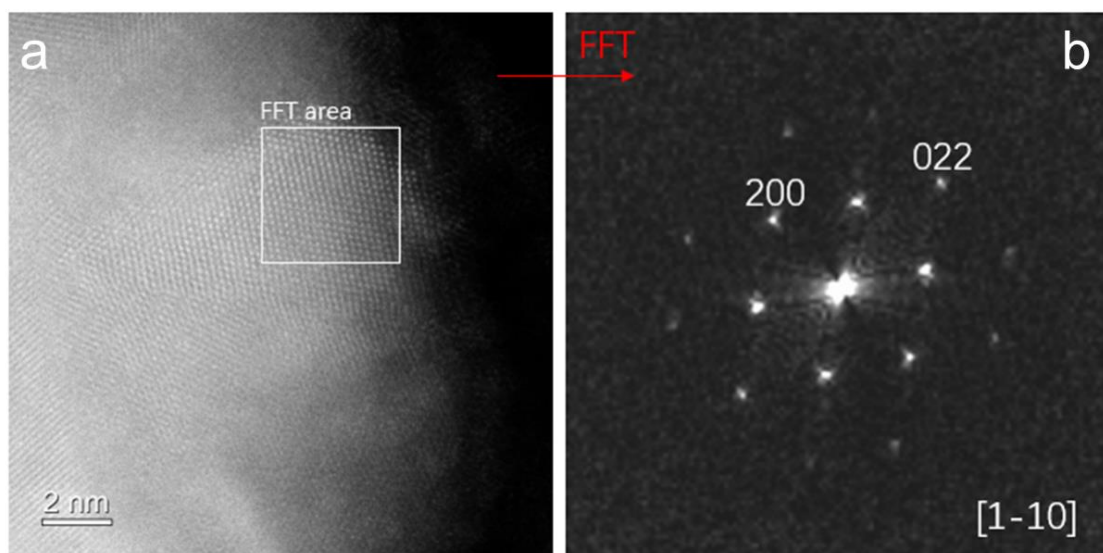
Supplementary Figure 7. (a) HRTEM image of Ni@C-MoO_x; (b) selected-area FFT pattern of area 1 in figure a; (c) selected-area FFT pattern of area 2 in figure a.



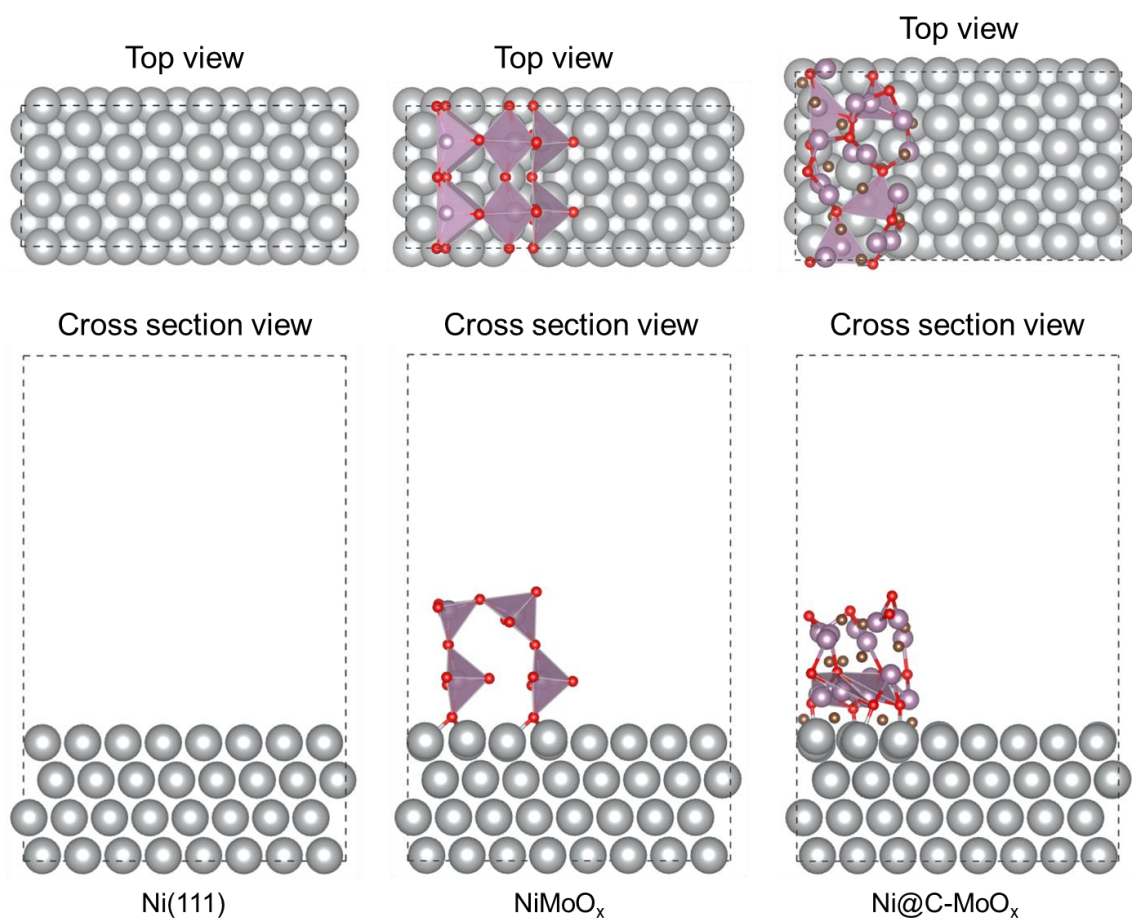
Supplementary Figure 8. Structural diagram and HRTEM of Ni@C-MoO_x (see Supplementary Note 12 for details).



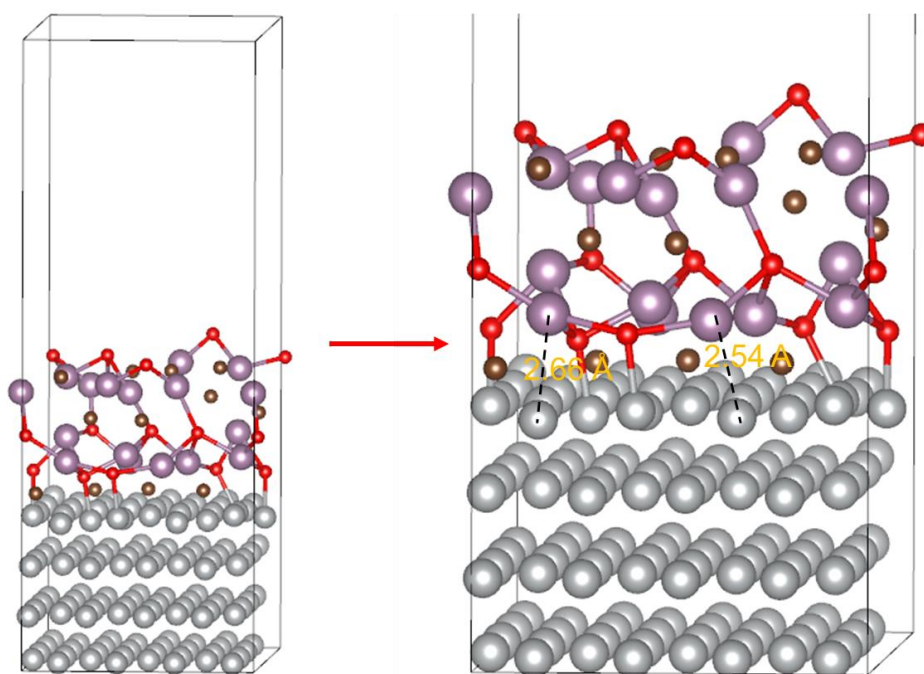
Supplementary Figure 9. STEM images of the Ni@C-MoO_x thin nanofilm.



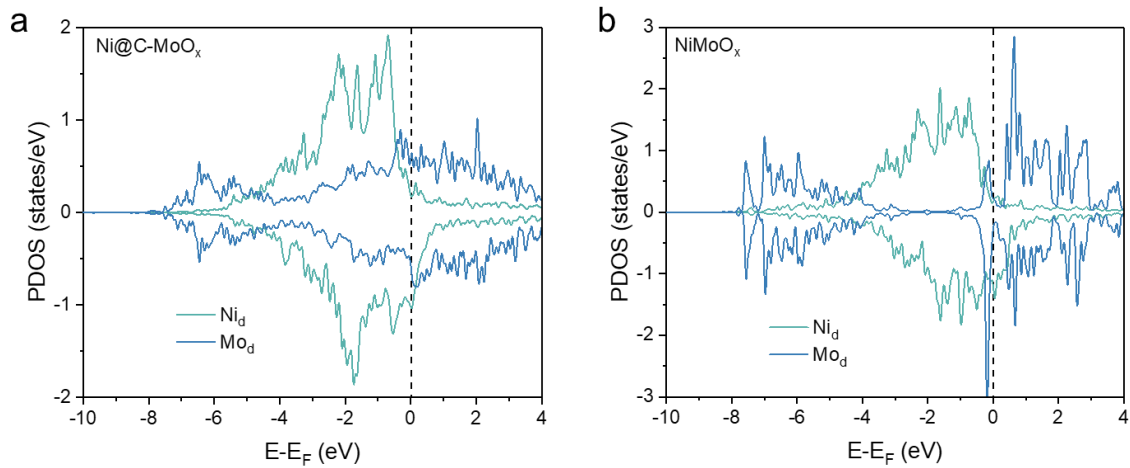
Supplementary Figure 10. (a) ADF-STEM image of Ni@C-MoO_x; (b) selected-area FFT pattern of area 1 in figure a.



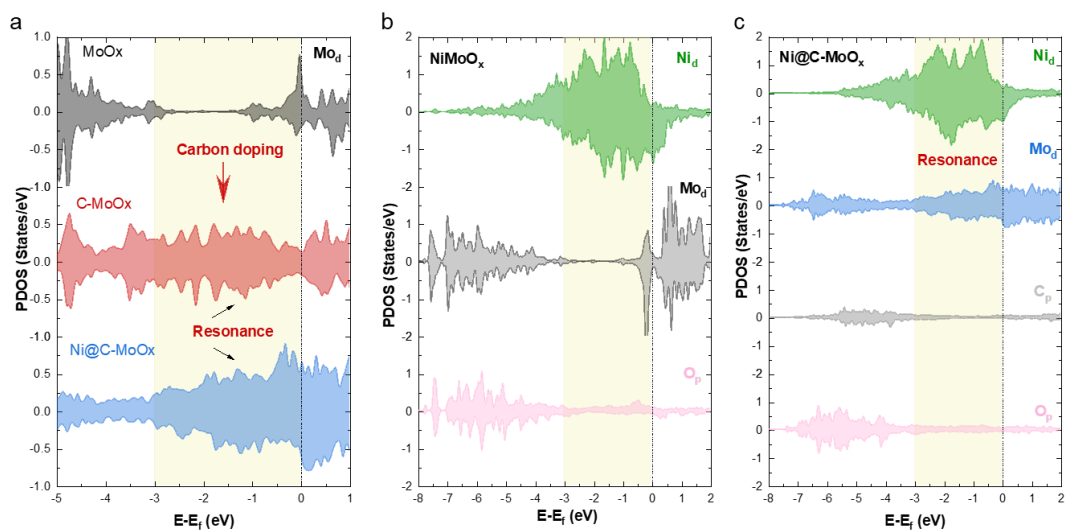
Supplementary Figure 11. Energy-optimized geometries of Ni(111), NiMoO_x and Ni@C-MoO_x models. Top and cross-section views are reported in the upper and bottom panels, Ni, Mo, O, C are represented by silver, purple, red and brown, respectively.



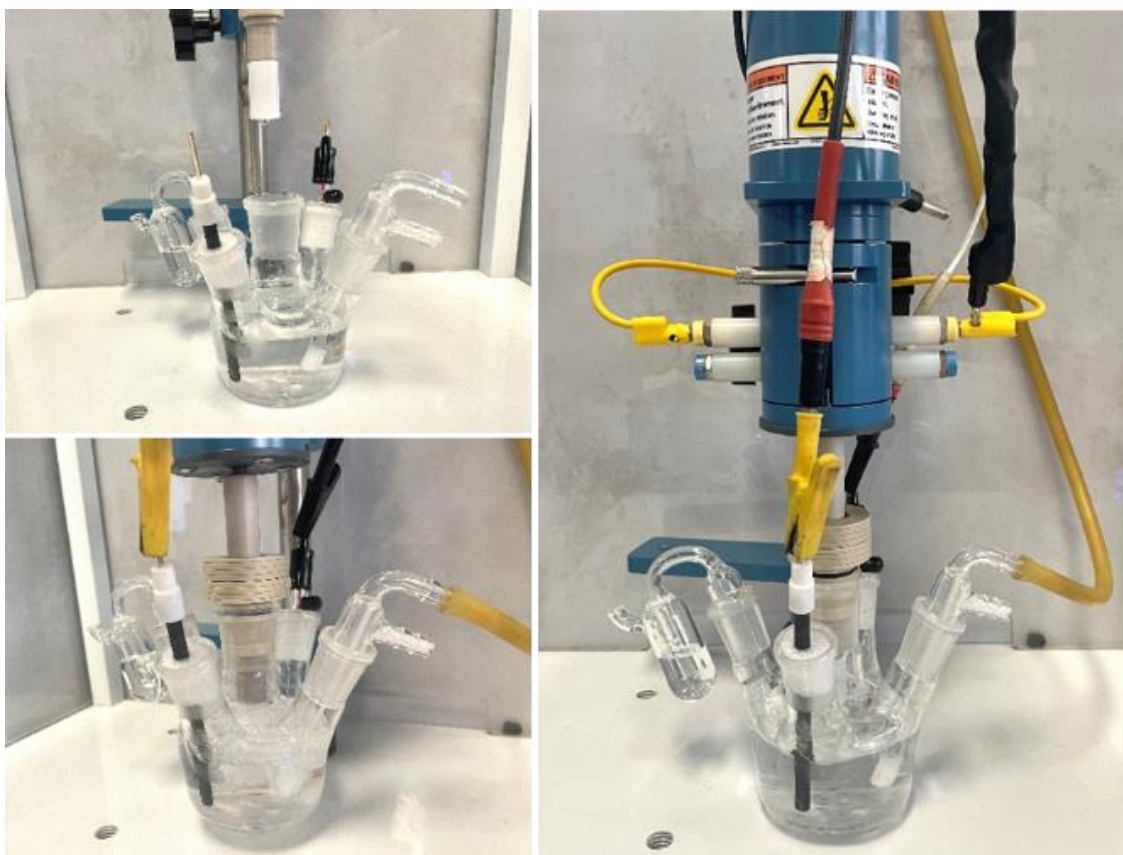
Supplementary Figure 12. DFT calculated Ball-and-stick model structure of Ni@C-MoO_x. As shown in Supplementary Figure 12, a Ni-Mo connection was spontaneously assembled after structural optimization. The atomic distance of Ni-Mo connection at the interface (2.54 Å) is in good agreement with the atomic distance of Ni-Mo observed by HRTEM.



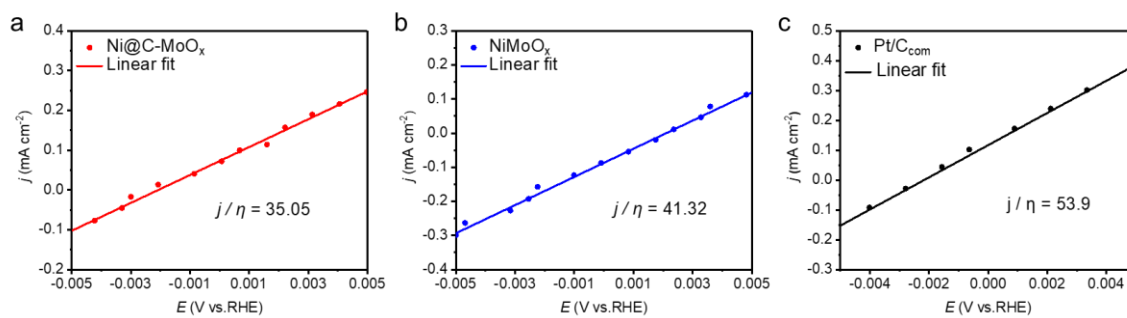
Supplementary Figure 13. (a) PDOS for Ni d and Mo d in Ni@C-MoO_x ; (b) PDOS for Ni d and Mo d in NiMoO_x .



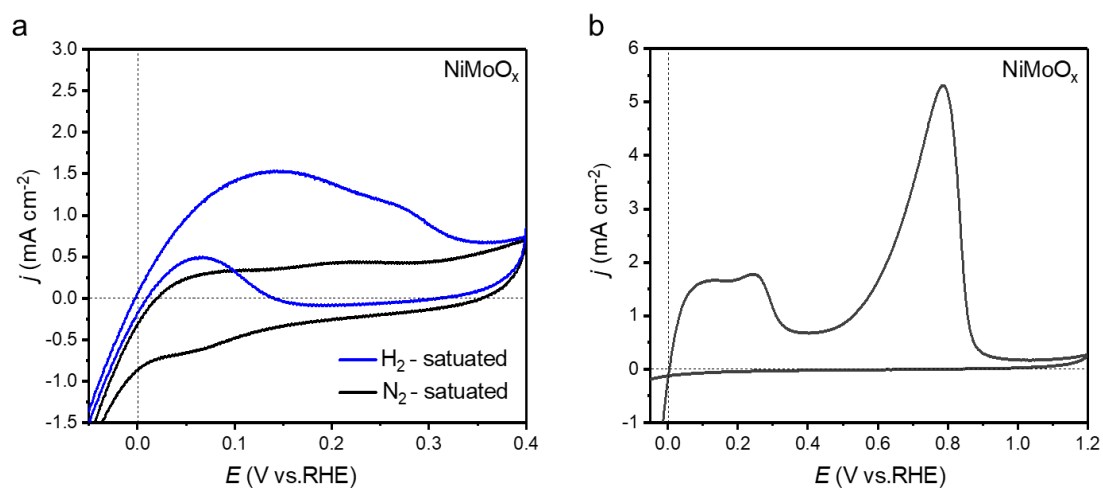
Supplementary Figure 14. The PDOS of the Mo_d, Ni_d, O_p and C_p for MoO_x, C-MoO_x, NiMoO_x and Ni@C-MoO_x.



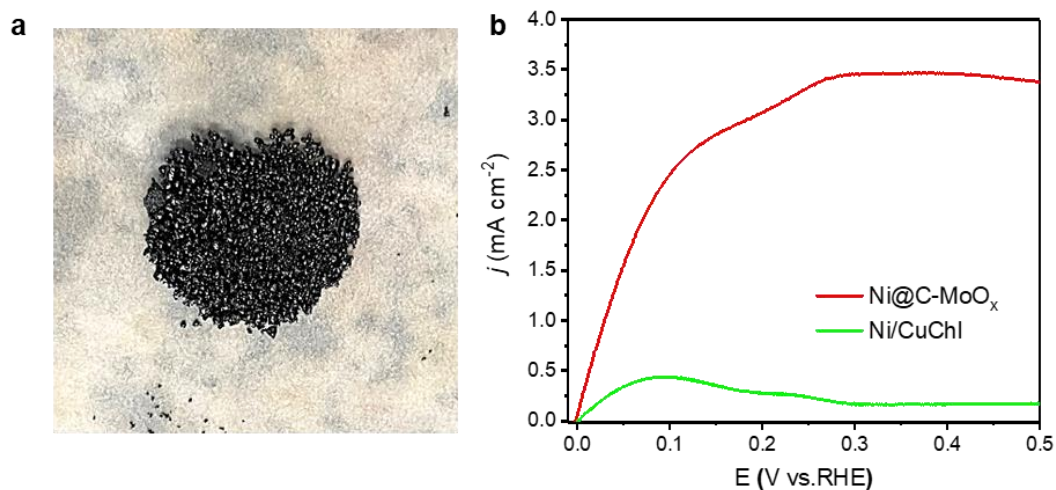
Supplementary Figure 15. Photographs of a three-electrode electrochemical cell with working electrode, reference electrode, counter electrode and gas inlet. The electrolytic cell of the three-electrode system used is shown on the right side. The glass container/cell used to hold the electrolyte has five ports; four side ports for reference electrode (calomel electrode), counter electrode (carbon rod), the gas inlet tube and the spherical bubble blower, and one central port for the working electrode. Each port is equipped with a sealing plug, which can be observed by a spherical bubbler to check the tightness of the connection¹.



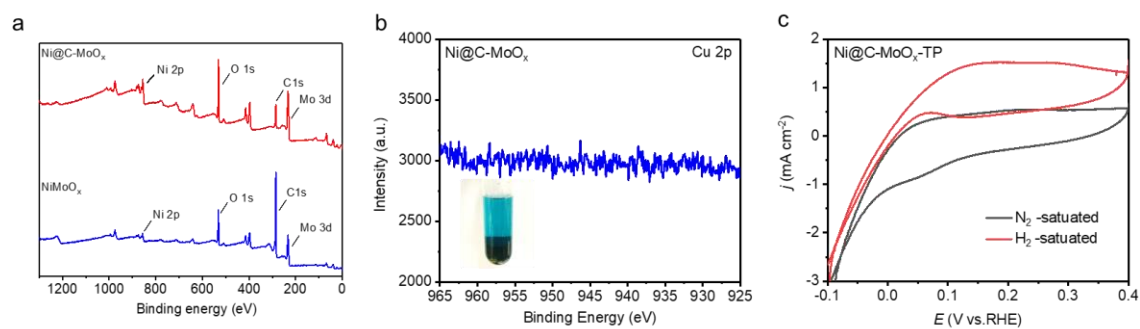
Supplementary Figure 16. (a) Micro-polarization curve of Ni@C-MoO_x; (b) Micro-polarization curve of NiMoO_x; (c) Micro-polarization curve of Pt/C. Micro-polarization method: In a small potential window of the micro-polarization region near the equilibrium potential (± 10 mV vs. RHE), j_k approximately equals to the measured current j , in this case, the Butler-Volmer equation can be expanded by Taylor's formula and simplified as $j = j_0 \eta F/RT$. Therefore, j_0 can be calculated from the slope of the linear fitting in the micro-polarization surface area². The calculated j_0 for Ni@C-MoO_x, NiMoO_x and Pt/C are 0.92 mA cm⁻²_{disk}, 1.08 mA cm⁻²_{disk} and 1.41 mA cm⁻²_{disk}.



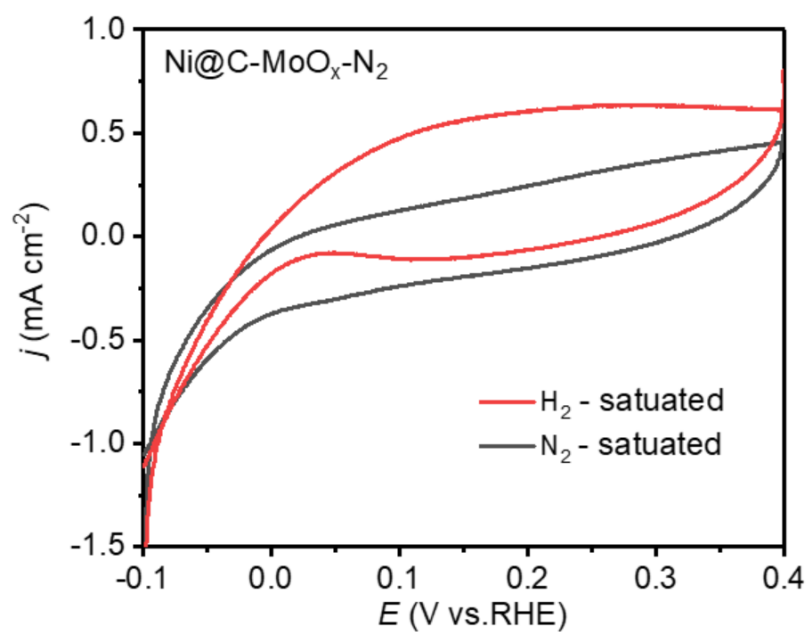
Supplementary Figure 17. Cyclic voltammograms recorded on NiMoO_x electrode in H_2 and N_2 -saturated 0.1 M KOH solution with the potential scanning from -0.05 V_{RHE} to (a) 0.4 V_{RHE} and (b) 1.2 V_{RHE}.



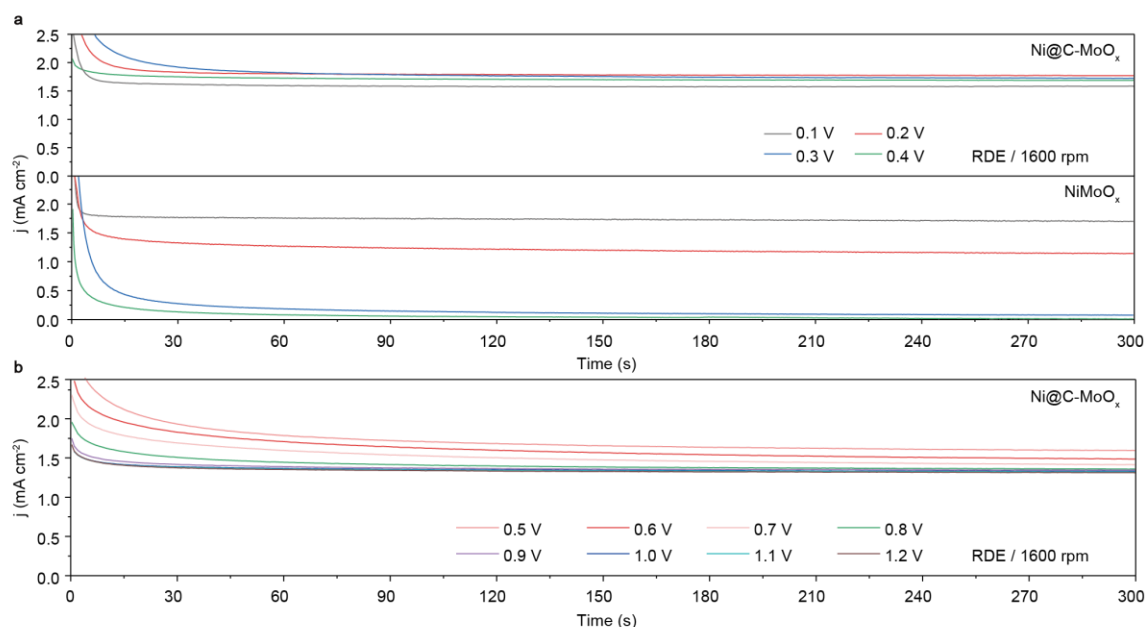
Supplementary Figure 18. (a) Photograph of Ni/CuChI synthesized in the same way as Ni@C-MoO_x except without Mo precursor; (b) The HOR polarization curves recorded on Ni@C-MoO_x and Ni/CuChI electrodes in H_2 -saturated 0.1 M KOH, data were obtained using a rotating disk electrode at a rotation rate of 2500 rpm and with a potential scan rate of 5 mV s^{-1} .



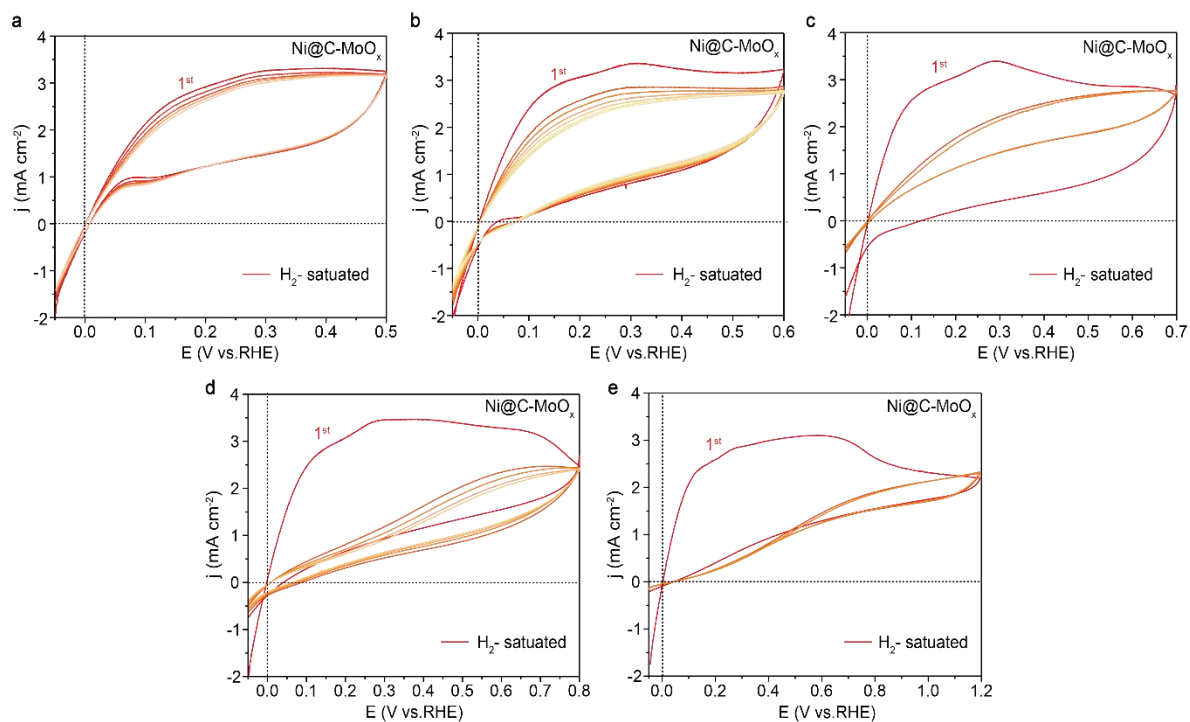
Supplementary Figure 19. (a) XPS spectra of Ni@C-MoO_x and NiMoO_x; (b) XPS spectra of Cu 2p in Ni@C-MoO_x; (c) Cyclic voltammograms recorded on Ni@C-MoO_x-TP electrode in H₂ and N₂-saturated 0.1 M KOH, data were obtained using a rotating disk electrode at a rotation rate of 2500 rpm and with a potential scan rate of 5 mV s⁻¹ (see Supplementary Note 13 for details).



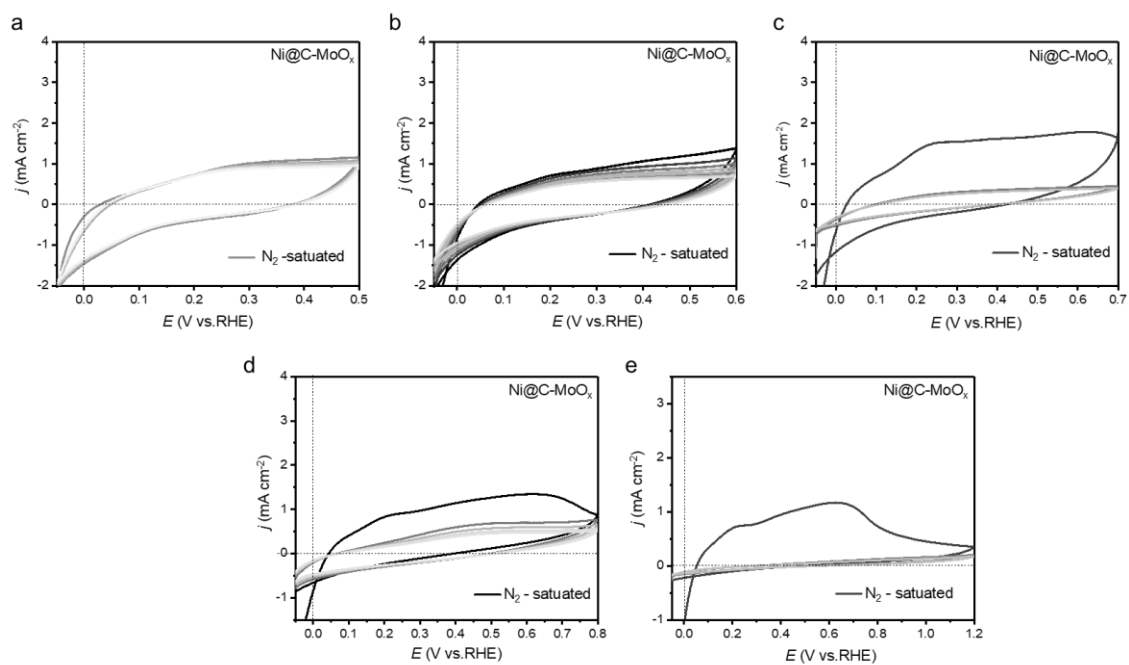
Supplementary Figure 20. Cyclic voltammograms of Ni@C-MoO_x-N₂ in H₂ and N₂-saturated 0.1 M KOH electrolyte with a rotating disk electrode at a rotation rate of 2500 rpm and a potential scan rate of 5 mV s⁻¹.



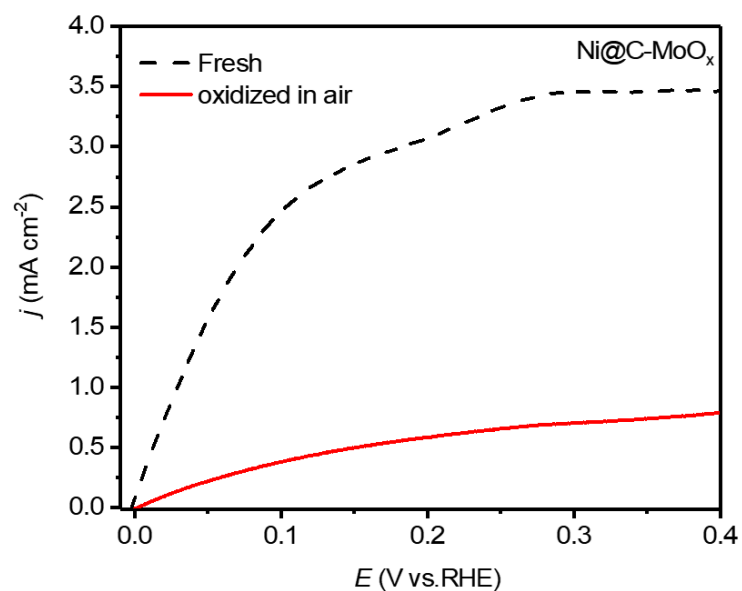
Supplementary Figure 21. (a) chronoamperometry curves obtained on Ni@C-MoO_x and NiMoO_x in H_2 -saturated 0.1 M KOH measured by using a rotating disk electrode with a rotation rate of 1600 rpm at 0.1 - 0.4 V_{RHE} ; (b) chronoamperometry curves obtained on Ni@C-MoO_x in H_2 -saturated 0.1 M KOH measured by using a rotating disk electrode with a rotation rate of 1600 rpm at 0.5 - 1.2 V_{RHE} .



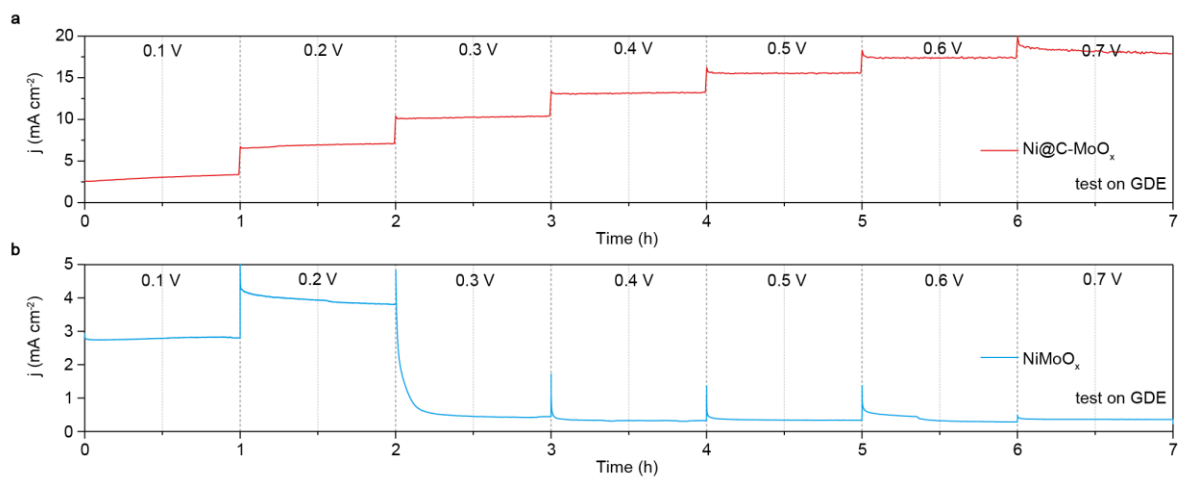
Supplementary Figure 22. Cyclic voltammograms recorded on Ni@C-MoO_x electrode in H₂-saturated 0.1 M KOH under different potential ranges, respectively. All data was recorded with a rotating disk electrode at a rotation rate of 2500 rpm and a potential scan rate of 5 mV s⁻¹.



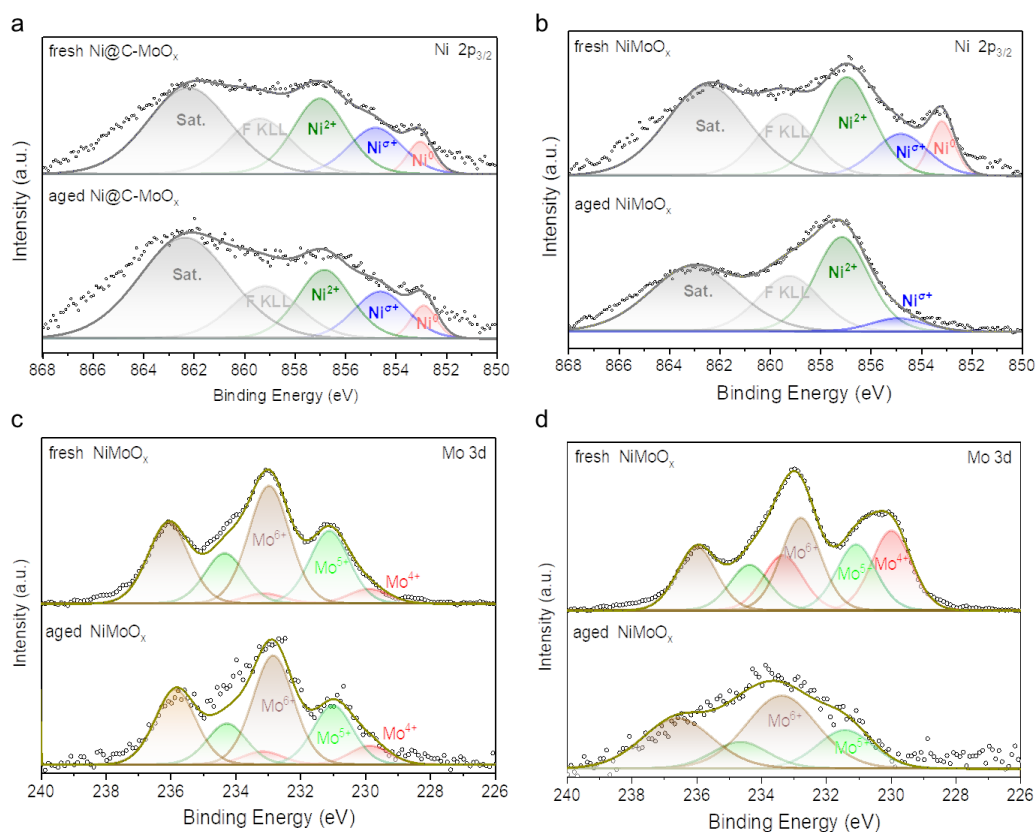
Supplementary Figure 23. Multi-cyclic voltammograms recorded on Ni@C-MoO_x electrode in N₂ - saturated 0.1 M KOH under different potential ranges, respectively. All data was recorded with a rotating disk electrode at a rotation rate of 2500 rpm and a potential scan rate of 5 mV s⁻¹.



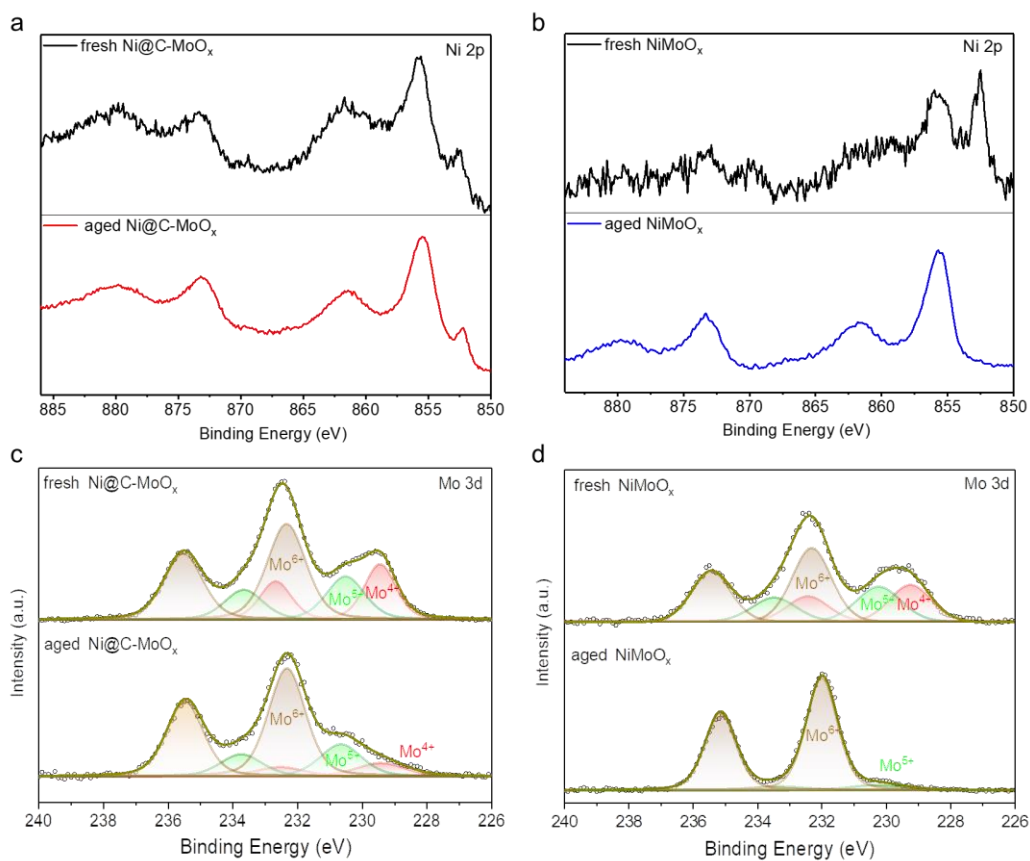
Supplementary Figure 24. The HOR polarization curves recorded on fresh and oxidized Ni@C-MoO_x electrodes in H₂-saturated 0.1 M KOH, data were obtained using a rotating disk electrode at a rotation rate of 2500 rpm and with a potential scan rate of 5 mV s⁻¹. Accelerated oxidation process: the catalyst modified electrode was baked/oxidized at 60 °C in air for 0.5 h.



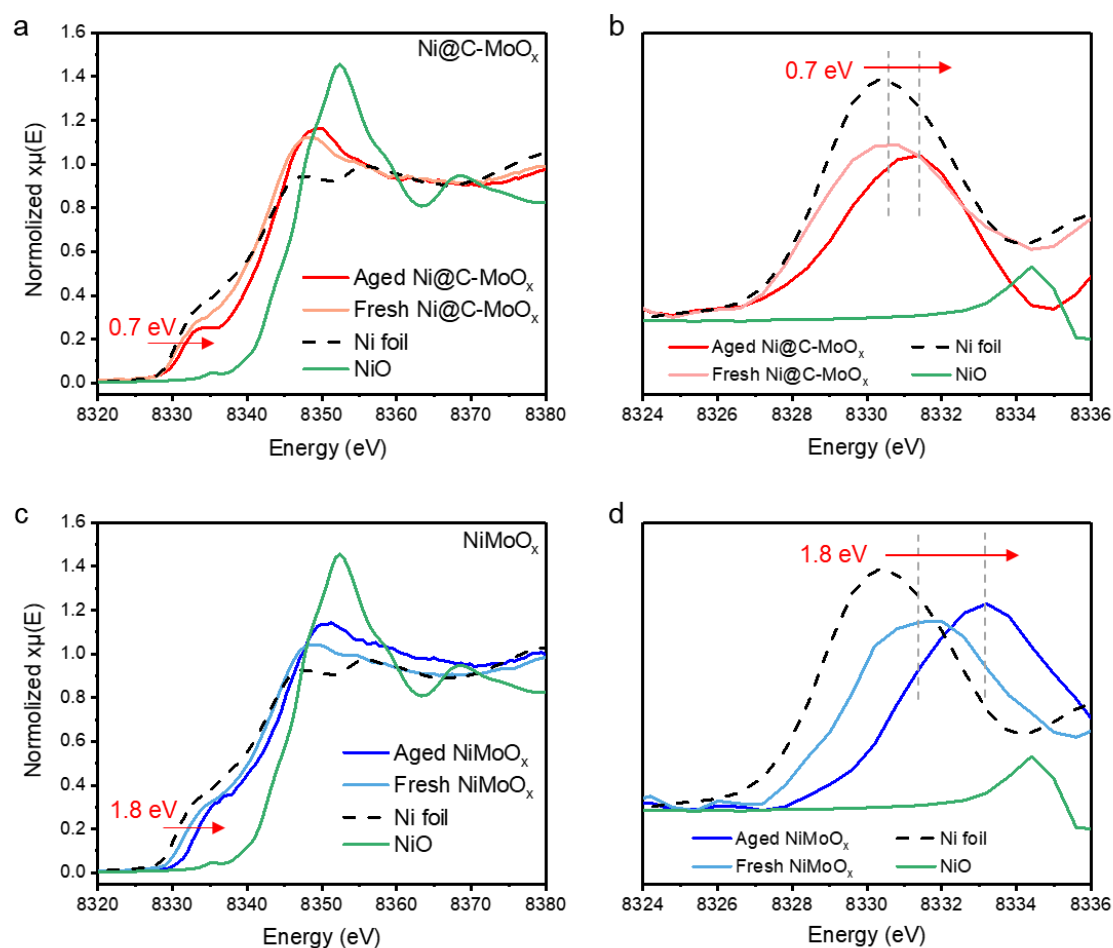
Supplementary Figure 25. Chronoamperometry curves recorded on Ni@C-MoO_x (a) and NiMoO_x (b) coated gas diffusion electrodes in H₂-saturated 0.1 M KOH at potentials stepped from 0.1 to 0.7 V_{RHE} .



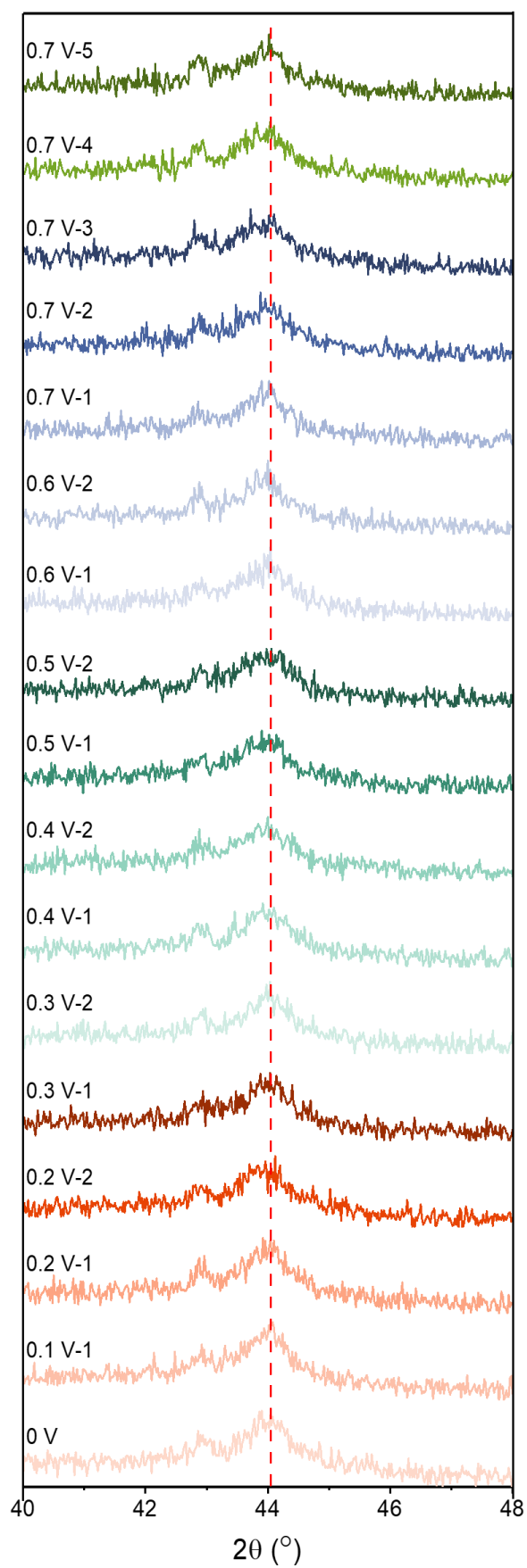
Supplementary Figure 26. XPS spectra of Ni 2p_{3/2} for (a) Ni@C-MoO_x and (b) NiMoO_x modified electrodes using Nafion as binder; XPS spectra of Mo 3d for (c) Ni@C-MoO_x and (d) NiMoO_x modified electrodes using Nafion as binder. The peak around 864 eV overlapped with the auger peak of F (KL2), as Nafion resin was used as binder for electrode preparation. However, the peak of Ni⁰ is not affected by F (KL2), and almost no change observed after stability test.



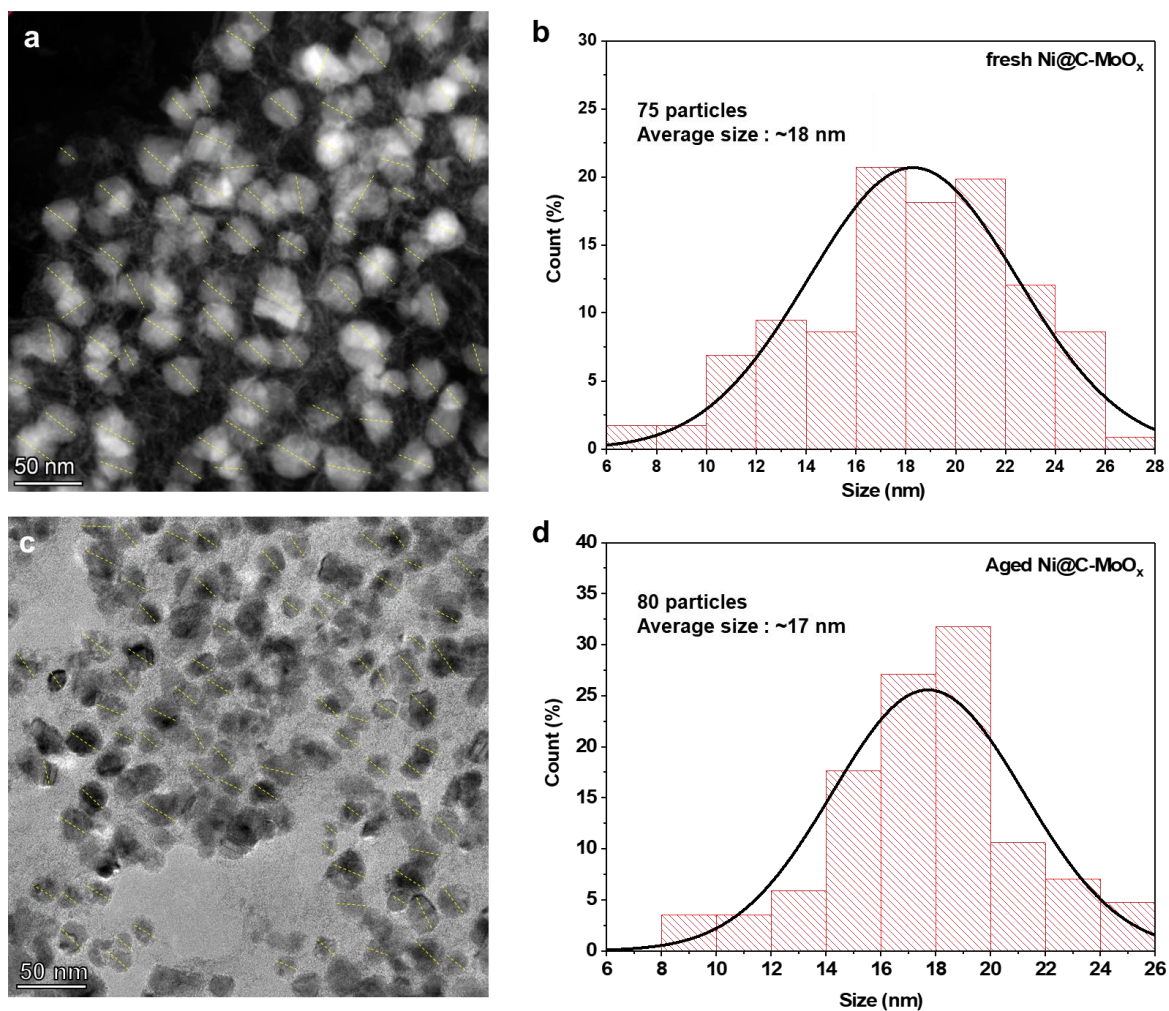
Supplementary Figure 27. XPS spectra of Ni 2p for (a) Ni@C-MoO_x and (b) NiMoO_x modified electrodes using QPCBP-10 ionomer as binder; XPS spectra of Mo 3d for (c) Ni@C-MoO_x and (d) NiMoO_x modified electrodes using QPCBP-10 ionomer as binder.



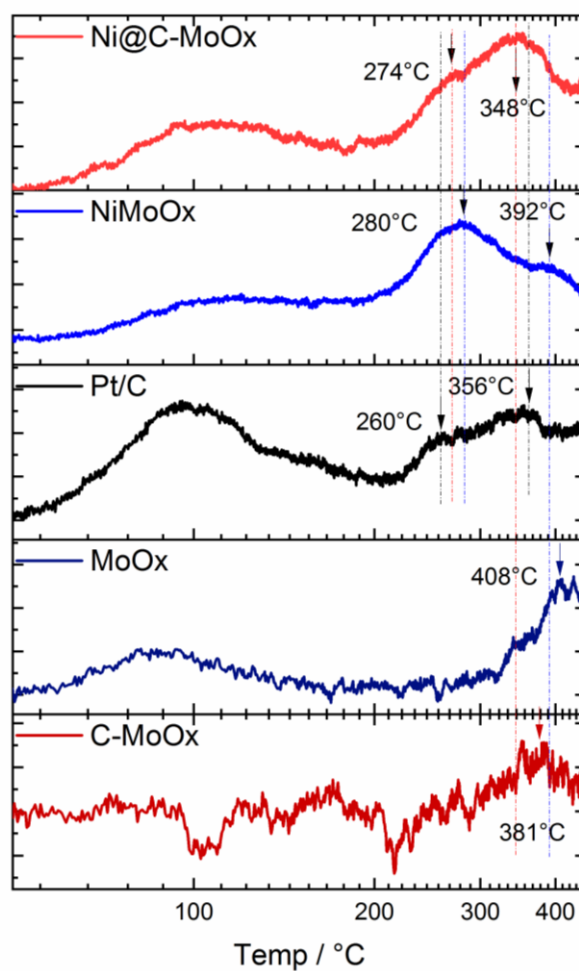
Supplementary Figure 28. (a) Normalized Ni K-edge XANES spectra of Ni@C-MoO_x before (named as fresh in the figure) and after (named as aged) step potential stability test; (b) the first derivative of figure a; (c) normalized Ni K-edge XANES spectra of NiMoO_x before and after stability test; (d) the first derivative of figure c.



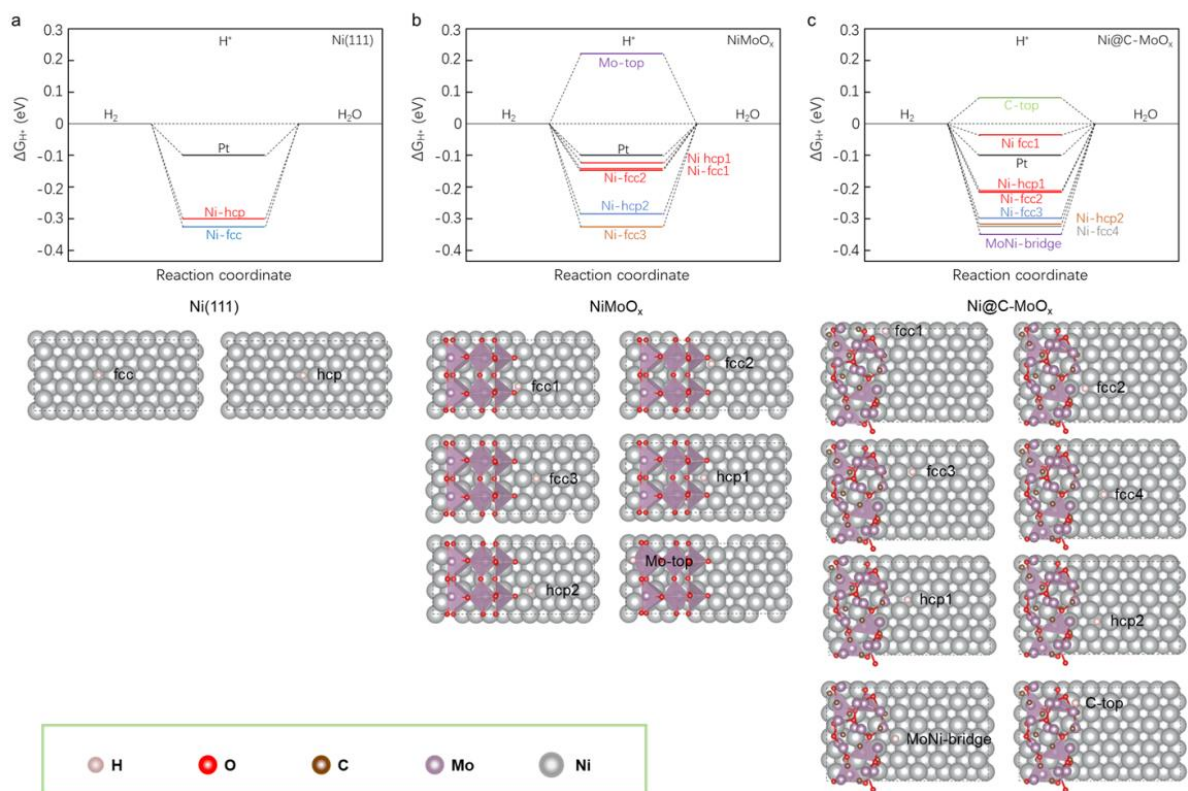
Supplementary Figure 29. In-situ XRD patterns of Ni@C-MoO_x at potentials around 0.1 - 0.7 V_{RHE} .



Supplementary Figure 30. (a) TEM image of fresh Ni@C-MoO_x; (b) particle size distribution of Ni NPs for fresh Ni@C-MoO_x; (c) TEM image of Ni@C-MoO_x after step potential test; (d) particle size distribution of Ni NPs for Ni@C-MoO_x after step potential test.



Supplementary Figure 31. H₂-TPD results for Ni@C-MoO_x, NiMoO_x, Pt/C_{com}, MoO_x and C-MoO_x.



Supplementary Figure 32. Hydrogen binding energy on Ni(111), NiMoO_x and Ni@C-MoO_x sites (see Supplementary Note 14 for details).

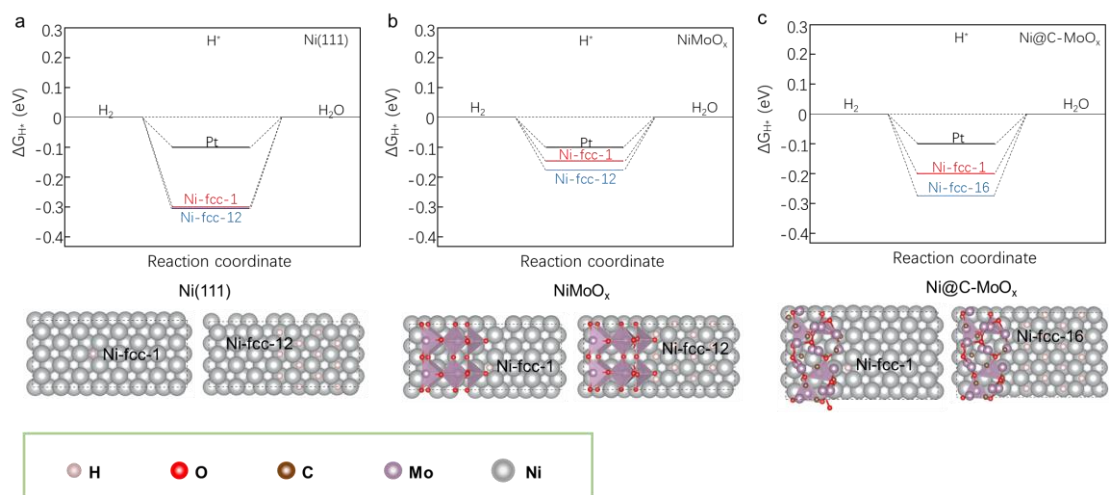


Figure 33. Hydrogen binding energy on Ni(111), NiMoO_x and Ni@C-MoO_x with a low and a high hydrogen coverages.

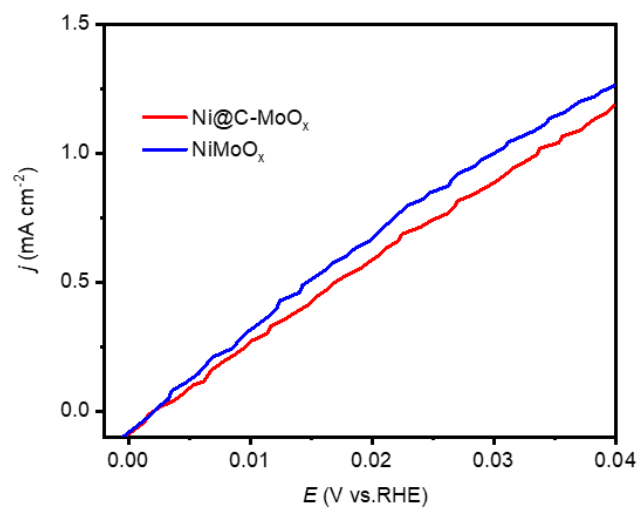
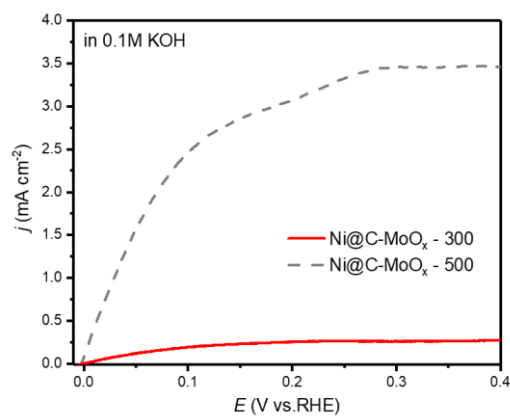
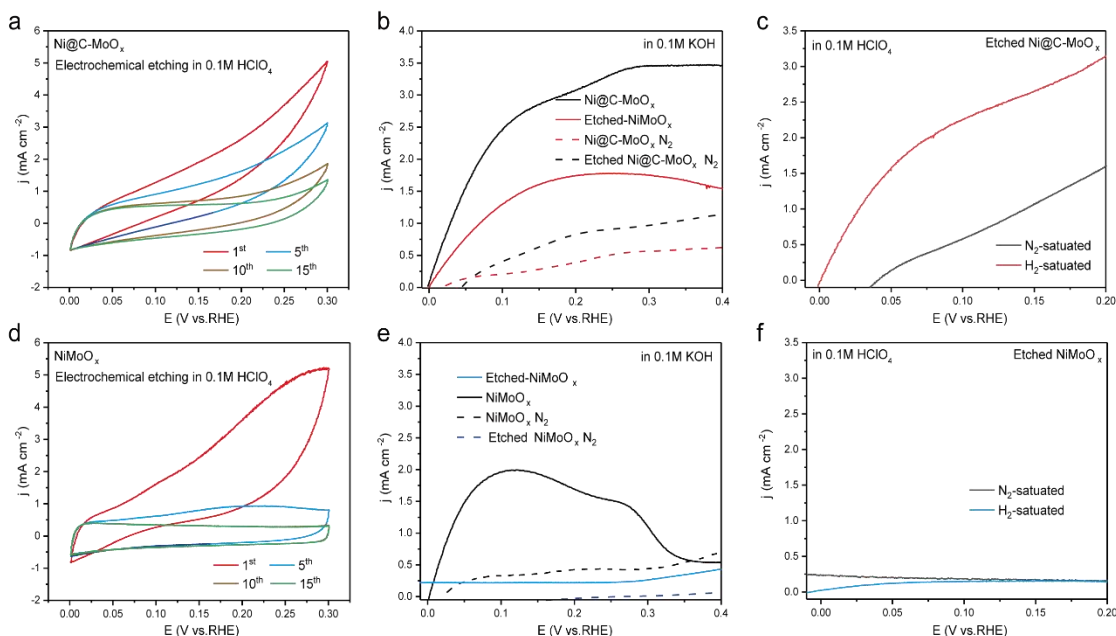


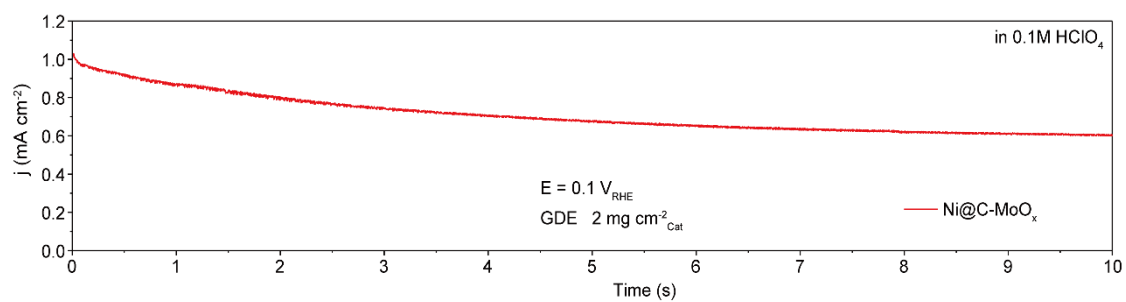
Figure 34. The HOR performance of Ni@C-MoO_x and NiMoO_x in H₂-saturated 0.1M KOH.



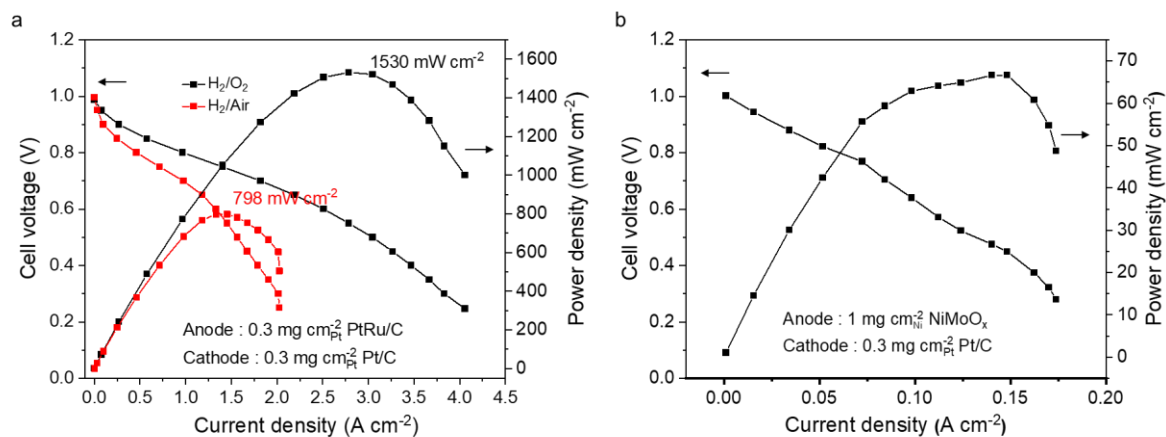
Supplementary Figure 35. The HOR polarization curves obtained on Ni@C-MoO_x catalysts that had been reduced at 300 °C (where no metallic Ni was formed) and 500 °C (where metallic Ni formed), respectively; the data were collected in H₂-saturated 0.1 M KOH electrolyte using a rotating disk electrode at a rotation rate of 2500 rpm and a potential scan rate of 5 mV s⁻¹.



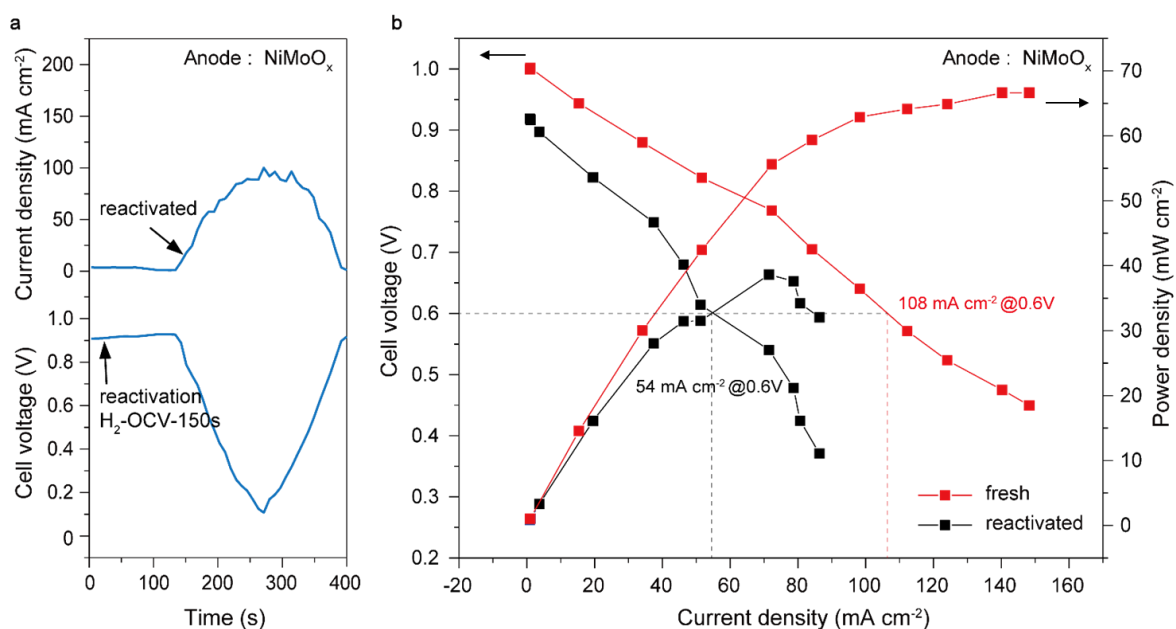
Supplementary Figure 36. Electrochemical etching. (a) Cyclic voltammograms recorded on Ni@C-MoO_x electrode in N₂-saturated 0.1 M HClO₄ with a potential scan rate of 10 mV s⁻¹; (b) HOR polarization curves recorded on Ni@C-MoO_x electrodes in H₂-saturated 0.1 M KOH, data obtained at a rotation rate of 2500 rpm with a potential scan rate of 5 mV s⁻¹; (c) HOR polarization curves recorded on Ni@C-MoO_x electrodes in H₂-saturated 0.1 M HClO₄, data obtained at a rotation rate of 2500 rpm with a potential scan rate of 5 mV s⁻¹; (d) Cyclic voltammograms recorded on NiMoO_x electrode in N₂-saturated 0.1 M HClO₄ with a scan rate of 10 mV s⁻¹; (e) HOR polarization curves recorded on NiMoO_x electrodes in H₂-saturated 0.1 M KOH, data obtained at a rotation rate of 2500 rpm with a potential scan rate of 5 mV s⁻¹; (f) HOR polarization curves recorded on NiMoO_x electrodes in H₂-saturated 0.1 M HClO₄, data obtained at a rotation rate of 2500 rpm with a potential scan rate of 5 mV s⁻¹.



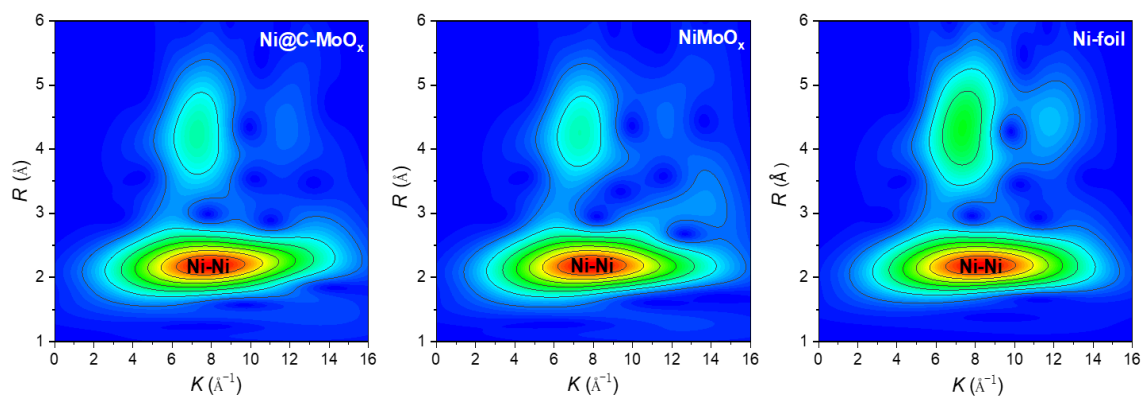
Supplementary Figure 37. Chronoamperometry curves recorded on Ni@C-MoO_x coated gas diffusion electrode (GDE) in H₂-saturated 0.1 M HClO₄ at 0.1 V_{RHE}.



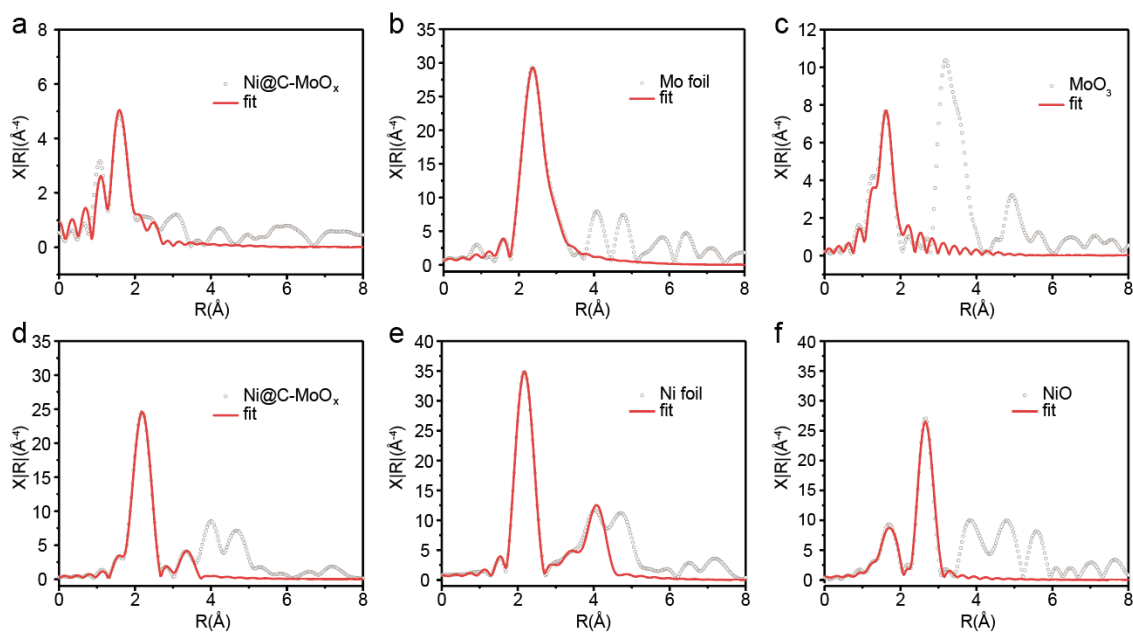
Supplementary Figure 38. (a) H₂/O₂ and H₂/air AEMFC performance testing using commercial PtRu/C_{com} as anode catalyst and 60% Pt/C_{com} as cathode catalyst. Test conditions: cell temperature 80 °C, cathode humidifier temperature 80 °C, anode humidifier temperature 80 °C, H₂ flow rate 0.5 l min⁻¹ and O₂/air flow rate 1.0 l min⁻¹ with a 200 kPa back pressure on both anode and cathode sides; (b) H₂/O₂ AEMFC performance using NiMoO_x as anode catalyst and 60% Pt/C_{com} as cathode catalyst, respectively. Test conditions: cell temperature at 80 °C, cathode humidifier at 80 °C, anode humidifier at 65 °C, H₂ flow rate of 0.5 l min⁻¹ and O₂ flow rate of 1.0 l min⁻¹ with 200 kPa back pressure at both anode and cathode sides.



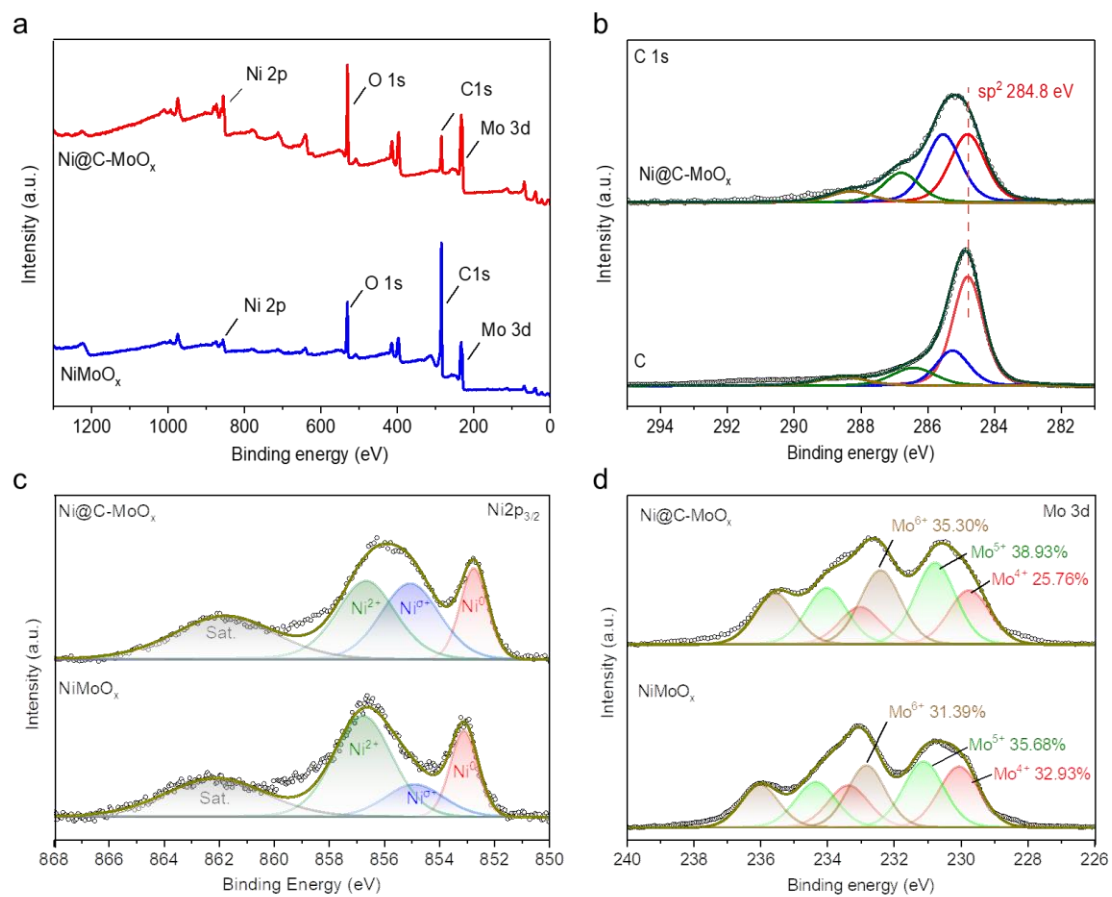
Supplementary Figure 39. (a) Reactivation operation for the deactivated NiMoO_x catalyst by feeding in H₂ for 150 s under open current voltage (OCV) at 80 °C; (b) H₂/O₂ AEMFC performance using NiMoO_x as the anode catalyst and Pt/C as the cathode catalyst. The fuel cell lost half of its power output after a single shutdown-start cycle of hydrogen shortage operation.



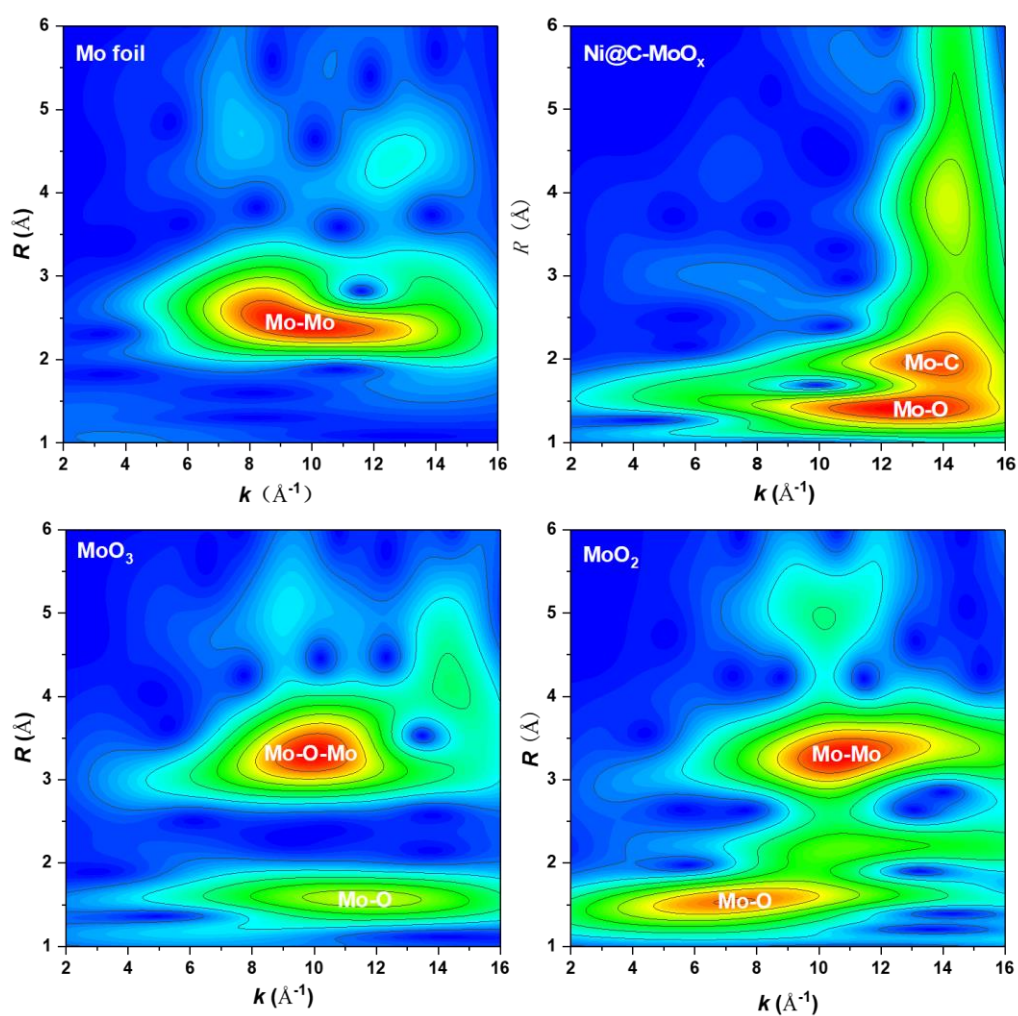
Supplementary Figure 40. Wavelet transform of k^3 -weighted EXAFS spectrum of the K-edge of Ni in Ni@C-MoO_x and that of two reference samples of NiMoO_x and Ni-foil for comparison.



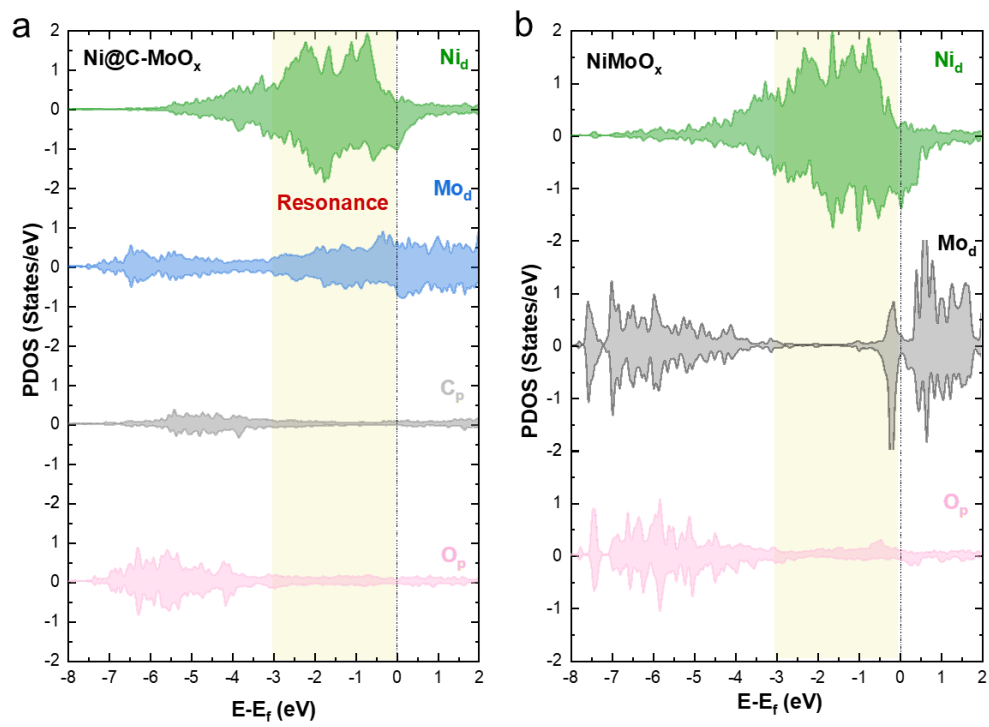
Supplementary Figure 41. Least-squares curve-fitting analysis of operando EXAFS spectra at the K-edge of Ni and Mo.



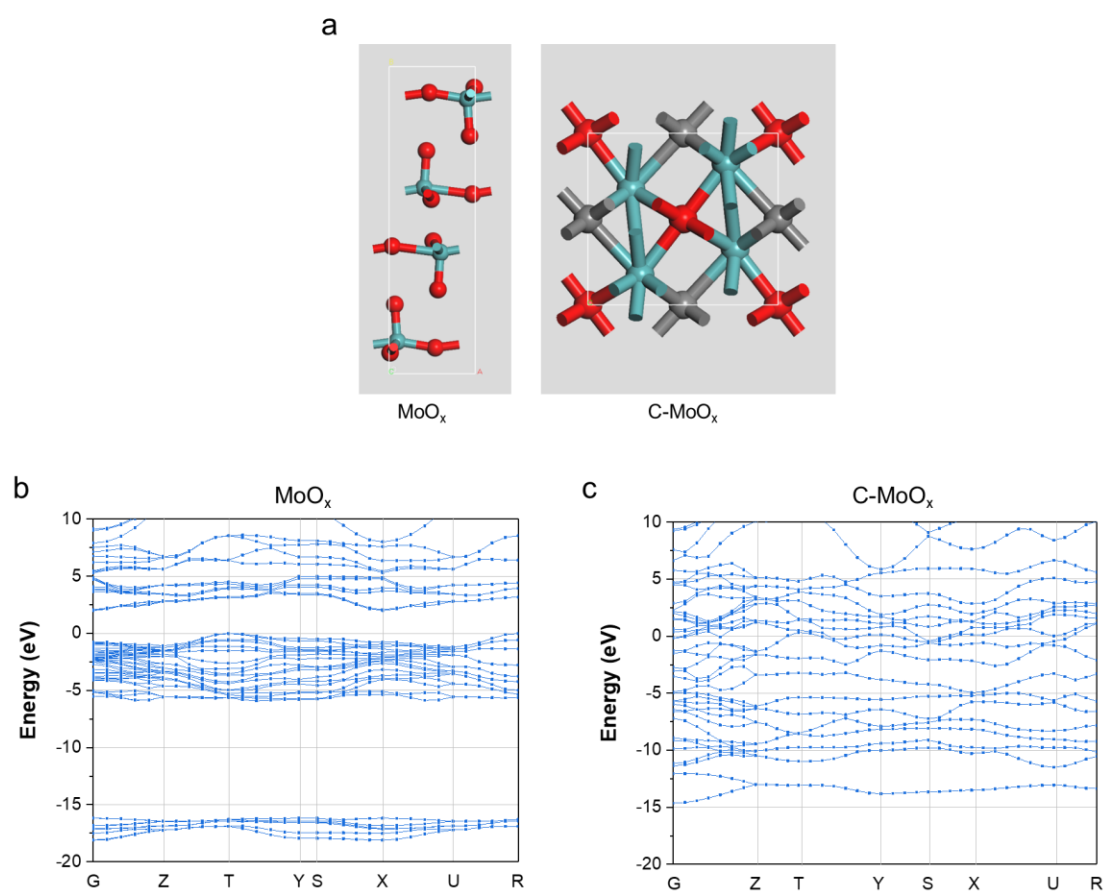
Supplementary Figure 42. XPS spectra recorded from the Ni@C-MoO_x and NiMoO_x catalysts.



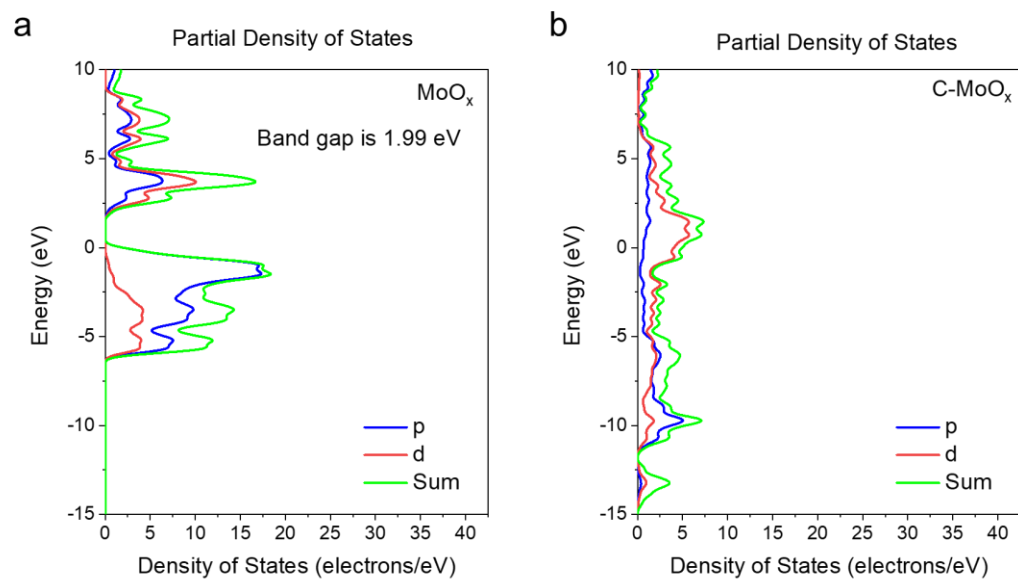
Supplementary Figure 43. Wavelet transform of k^3 -weighted EXAFS spectrum of the k-edge of Mo in Ni@C-MoO_x and that of three reference samples of Mo-foil, MoO₂ and MoO₃ for comparison.



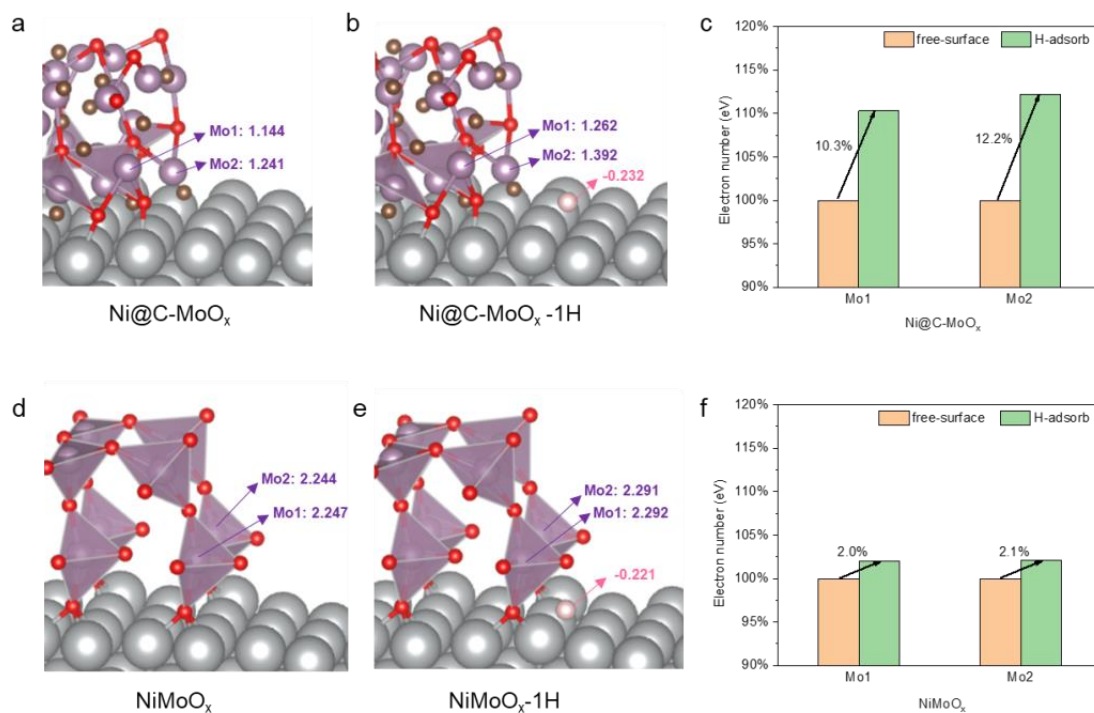
Supplementary Figure 44. PDOS of the surface O_p in $Ni@C-MoO_x$ and $NiMoO_x$.



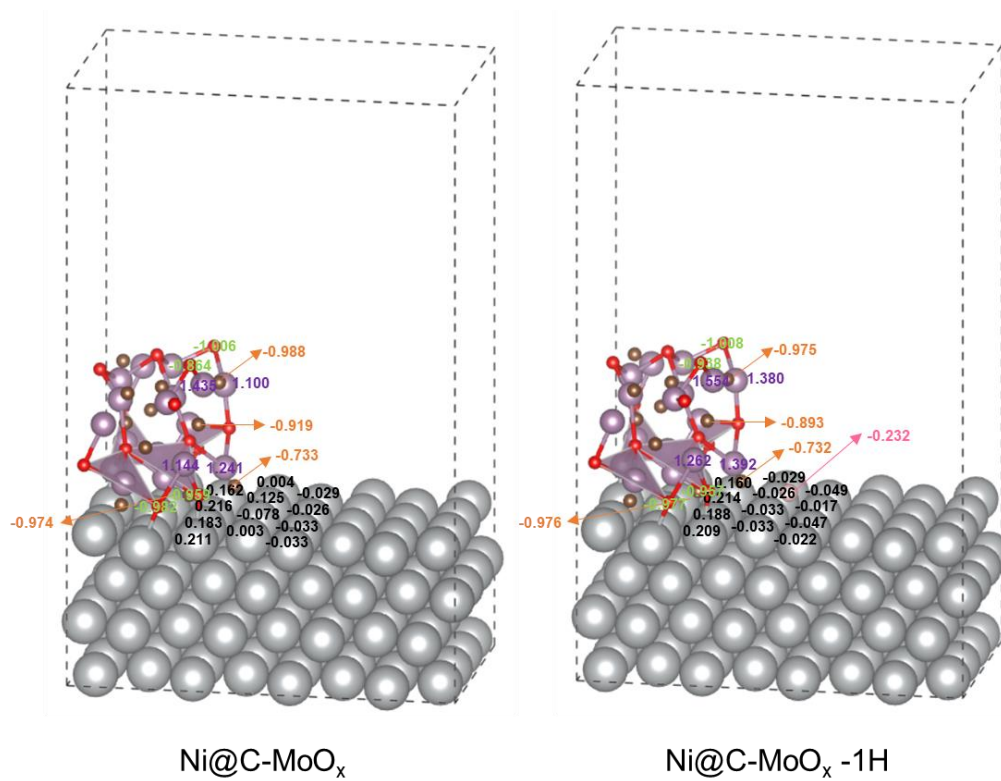
Supplementary Figure 45. (a) The primitive cell model of MoO_x and C-MoO_x; (b-c) the calculated band structure of (b) MoO_x and (c) C-MoO_x.



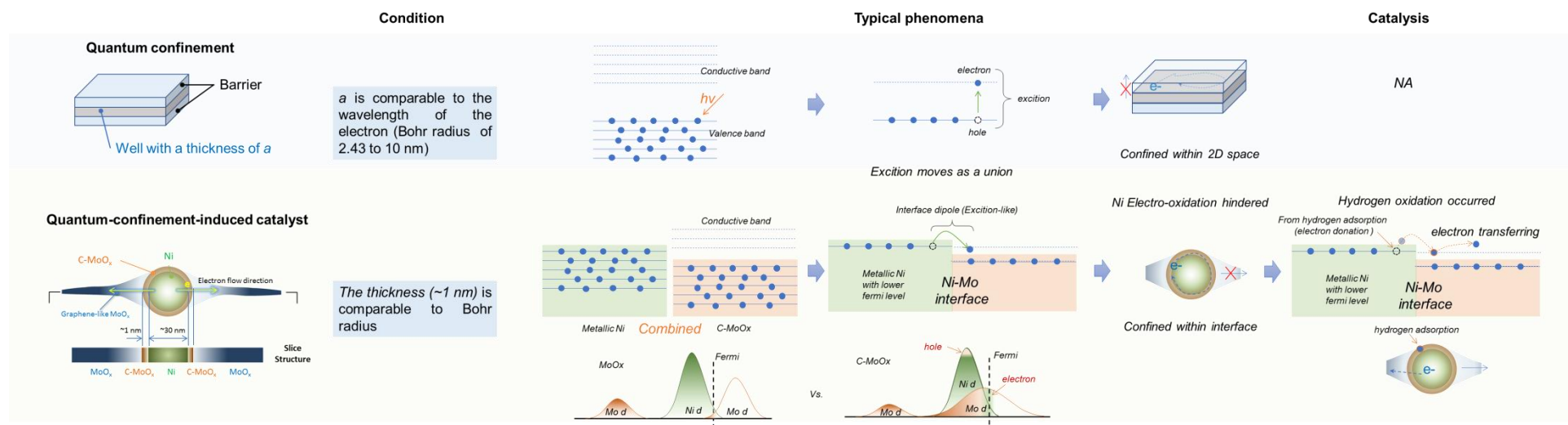
Supplementary Figure 46. The PDOS of MoO_x and C-MoO_x .



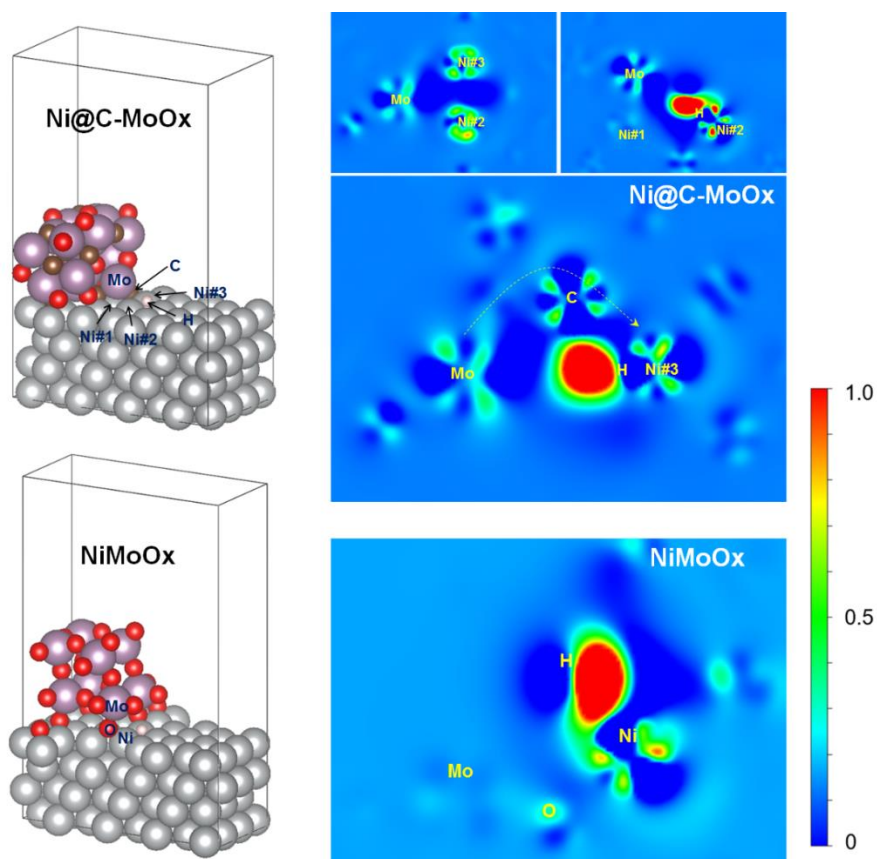
Supplementary Figure 47. The charge quantities of the interface Mo atoms in Ni@C-MoO_x and NiMoO_x and those after H adsorption (see Supplementary Note 15 for details).



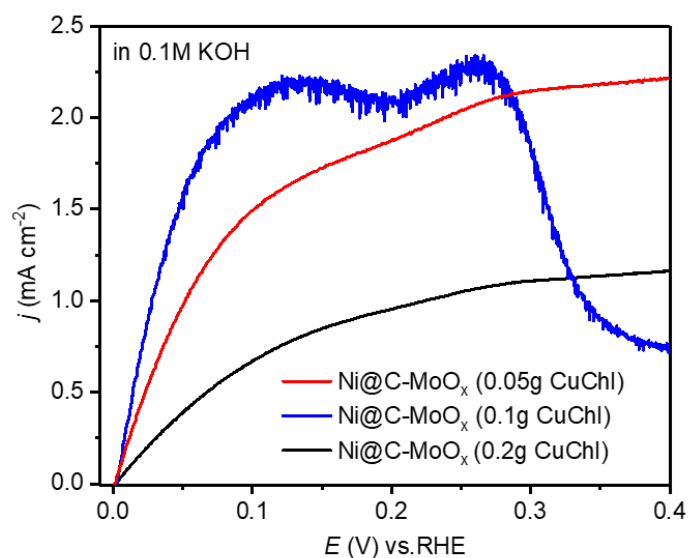
Supplementary Figure 48. The charge quantities for various atoms in Ni@C-MoO_x and those after H adsorption.



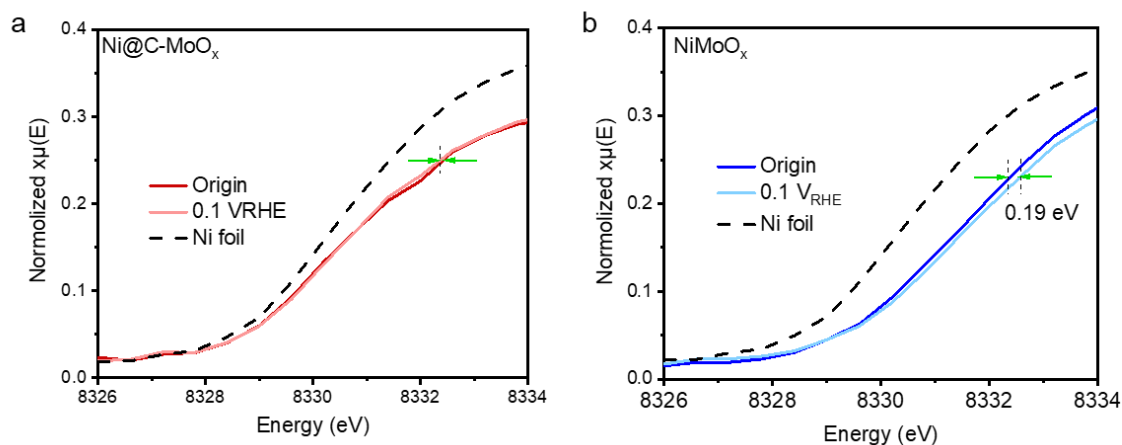
Supplementary Figure 49. Schematic diagram of electron confinement and transfer process (see Supplementary Note 16 for details).



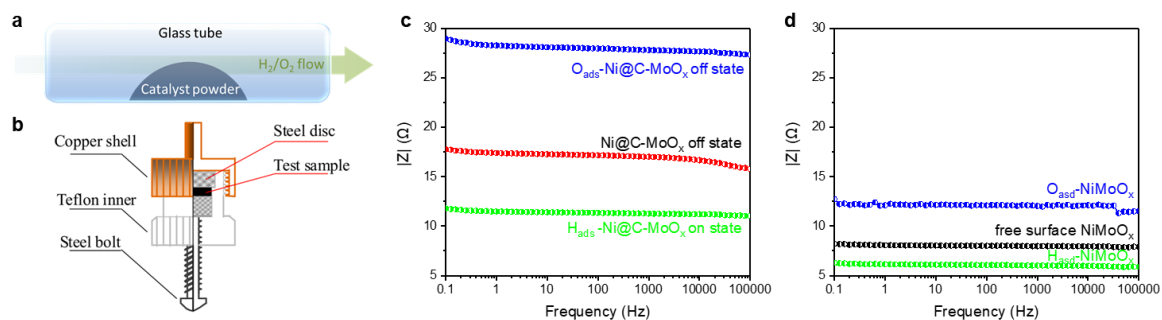
Supplementary Figure 50. The differential charge densities for Ni@C-MoO_x and NiMoO_x .



Supplementary Figure 51. The HOR polarization curves obtained on three Ni@C-MoO_x catalysts prepared with different amounts of CuChl in the precursors, the data were recorded in H₂-saturated 0.1 M KOH using a rotating disk electrode at a rotation rate of 1600 rpm, and a potential scan rate of 5 mV s⁻¹. The Ni@C-MoO_x catalysts at different degrees of confinement were synthesized by increasing or decreasing the addition of carbon precursor. As shown in Supplementary Figure 52, increasing carbon doping enhanced the protection against Ni oxidation but led to a weakened HOR performance. Decreasing the carbon addition, however, weakened the quantum confinement leading to an enhanced HOR performance and a weakened protection against Ni oxidation. These results further proved the relevant of quantum confinement to catalysis.



Supplementary Figure 52. The in-situ near edge X-ray absorption structure (NEXAS) spectra of Ni-k-edge for Ni@C-MoO_x (a) and NiMoO_x (b) in 0.1 M KOH under HOR condition. The in-situ NEXAS test were conducted in a polytetrafluoroethylene (PTFE) electrochemical cell containing Ni@C-MoO_x coated carbon paper as the working electrode, carbon rod as the counter electrode, and Hg/HgO electrode as the reference electrode. The electrochemical cell was assembled with 0.1 M KOH solution as the electrolyte. The NEXAS spectroscopy in the stability test for Ni was carried out using the RapidXAFS 2M at room temperature during chrono-current test under 0.1 V_{RHE} with continuous H₂ injecting into the electrolyte.



Supplementary Figure 53. (a) The glass tube used to pre-adsorb hydrogen or oxygen on catalyst powder; (b) Home-made powder resistance test device; (c) Electrochemical impedance spectroscopy (EIS) of 30 mg $Ni@C-MoO_x$ sample before gas adsorption (named free surface) and after H_2/O_2 adsorption (named as $H_{ads}/O_{ads}-Ni@C-MoO_x$). H_2/O_2 -adsorption: $Ni@C-MoO_x$ powder was put in a H_2/O_2 purged-tube for 30 min before impedance test, respectively; (d) EIS of 30 mg $NiMoO_x$.

Supplementary Table 1. The atomic ratios in the Ni@C-MoO_x as detected by XPS and EDX.

Element	XPS (at%)	XPS ratio ^a	EDX (at%)	EDX ratio ^b
Mo	11.97	1	8.20	1
Ni	8.73	0.73	24.62	3.00
O	39.09	3.26	21.73	2.65
C	40.21	3.36	45.35	5.53

^aXPS ratio: The atomic ratio of Mo from XPS was used to normalize all the other elements; ^bEDX ratio: The atomic ratio of Mo from EDX was used to normalize all the other elements.

Supplementary Table 2. The comparison of j_0 calculated by micro-polarization method.

Samples	j_0 from Micro-polarization (mA cm _{disk} ⁻²)
Ni@C-MoO _x	0.92
NiMoO _x	1.08
Pt/C _{com}	1.41

Supplementary Table 3. The comparison of the real surface activity of Ni and Pt nanoparticles.

Sample	Particle Size (nm)	Metal loading (mg disk ⁻¹)	Density (g cm ⁻³)	V (cm ³)	S (cm ²)	j ₀ mA disk ⁻²	SA ^a mA cm ⁻²
Ni@C-MoO _x	~30 nm	0.030	8.90	3.37*10 ⁻⁶	6.74	0.18	0.03
Pt/C _{com}	~3 nm	0.005	21.45	2.3*10 ⁻⁷	4.60	0.28	0.06

SA^a: The real surface area activity, SA = j₀ / S.

Supplementary Table 4. The fitting result of the XPS spectra for Ni in Ni@C-MoO_x and NiMoO_x (Nafion was used as binder).

Sample	Name	Peak BE (eV)	FWHM (eV)	Atomic (%)
Fresh Ni@C-MoO _x	Ni ⁰	853.06	1.17	12.09
	Ni ^{σ+}	854.79	2.50	32.34
	Ni ²⁺	856.99	2.50	55.56
Aged Ni@C-MoO _x	Ni ⁰	852.88	1.17	11.46
	Ni ^{σ+}	854.60	2.50	34.90
	Ni ²⁺	856.81	2.50	53.63
Fresh NiMoO _x	Ni ⁰	853.18	1.17	15.04
	Ni ^{σ+}	854.80	2.50	24.68
	Ni ²⁺	856.94	2.50	60.27
Aged NiMoO _x	Ni ⁰	NA	NA	0
	Ni ^{σ+}	854.80	2.50	15.37
	Ni ²⁺	857.12	2.50	84.63

Supplementary Table 5. The fitting result of the XPS spectra for Ni in Ni@C-MoO_x and NiMoO_x (QPCBP-10 ionomer was used as binder).

Sample	Name	Peak BE (eV)	FWHM (eV)	Atomic (%)
Fresh Ni@C-MoO _x	Ni ⁰	852.62	1.17	16.38
	Ni ^{σ+}	855.07	2.50	33.86
	Ni ²⁺	856.11	2.50	49.76
Aged Ni@C-MoO _x	Ni ⁰	852.62	1.17	12.29
	Ni ^{σ+}	855.34	2.50	34.85
	Ni ²⁺	856.17	2.50	54.87
Fresh NiMoO _x	Ni ⁰	852.99	1.17	31.99
	Ni ^{σ+}	854.97	2.50	17.46
	Ni ²⁺	856.34	2.50	50.55
Aged NiMoO _x	Ni ⁰	NA	NA	0
	Ni ^{σ+}	856.17	2.50	100

Supplementary Table 6. Ni content in Ni@C-MoO_x and NiMoO_x catalysts obtained by ICP-OES methods.

Samples		Ni content	
		(wt%)	(ac%)
Ni@C-MoO _x	fresh	44.2	26.0
	etched	26.8	15.7
NiMoO _x	fresh	44.3	26.0
	etched	2.1	1.23

Supplementary Table 7. Comparison of peak power density of AEMFCs operated with Ni-based anodes.

Anode catalyst	Cathode catalyst	Peak power density (mW cm ⁻²)		Specific peak power density (mW mg _{Ni} ⁻¹)	Cell temp (°C)	Backpressure (anode/cathode, kPa)	References
Ni@C-MoO _x 1 mg _{Ni} cm ⁻²	Pt/C 0.3 mg _{Pt} cm ⁻²	H ₂ /O ₂ H ₂ /air	486 400	486 400	80	200/200	This work
Ni@CN _x 15 mg _{Ni} cm ⁻²	Pt/C 0.4 mg _{Pt} cm ⁻²	H ₂ /O ₂ H ₂ /air	480 360	32 24	80	200/200	<i>Proc. Natl. Acad. Sci.</i> 2022, 119 , e2119883119
Ni-H ₂ -NH ₃ 6 mg _{Ni} cm ⁻²	Pt/C 0.4 mg _{Pt} cm ⁻²	H ₂ /O ₂ H ₂ /air	628 500	105 83	90	250/250	<i>Nat. Mater.</i> 2022, 21 , 804-810
Co-MoNi ₄ 2 mg _{Ni} cm ⁻²	Pt/C 0.4 mg _{Pt} cm ⁻²	H ₂ /O ₂ H ₂ /air	525 390	263 195	95	200/200	<i>Angew. Chem. Int. Ed.</i> 2022, 61 , e202208040
Ni ₅₂ Mo ₁₃ Nb ₃₅ 2 mg _{Ni} cm ⁻²	Pt/C 0.4 mg _{Pt} cm ⁻²	H ₂ /O ₂ H ₂ /air	390 253	195 126	90	200/200	<i>Nat. Catal.</i> 2022, 5 , 993-1005
Ni@O _r -Ni 1.3 mg _{Ni} cm ⁻²	Pt/C 0.4 mg _{Pt} cm ⁻²	H ₂ /O ₂	274	211	80	200/200	<i>J. Am. Chem. Soc.</i> 2022, 144 , 12661-12672
Ni@C 5 mg _{Ni} cm ⁻²	Pt/C 0.4 mg _{Pt} cm ⁻²	H ₂ /O ₂	160	32	80	200/200	<i>ACS Appl. Mater. Int.</i> 2020, 12 , 28, 31575
NiCu/KB 5 mg _{Ni} cm ⁻²	Pd/XC72R 0.2 mg _{Pd} cm ⁻²	H ₂ /O ₂	350	70	80	140/140	<i>J. Mater. Chem. A</i> 2017, 5 , 24433
NiMo/KB 4 mg _{Ni} cm ⁻²	Pt/C 0.2 mg _{Pt} cm ⁻²	H ₂ /O ₂	120	30	70	140/140	<i>Sustain. Energy Fuels</i> 2018, 2 , 2268-2275
Ni ₄ Mo/TiO ₂ 1.35 mg _{Ni} cm ⁻²	Pt/C 0.4 mg _{Pt} cm ⁻²	H ₂ /O ₂	520	385	80	200/200	<i>Nat Commun.</i> 2024, 15 , 76

Supplementary Table 8. Structural parameters obtained from the curve-fitting analysis of the EXAFS spectra.

Sample (s0 = 0.85)	Path	CN^a	R(Å)^b	σ² (10³Å²)^c	ΔE₀ (eV)^d	R factor
Ni@C-MoO_x	Ni-Ni	0.82±0.07	2.50±0.06	7.7	7.0	0.015
	Ni-O	0.69±0.28	3.81±0.05	6.5	9.0	
NiMoO_x	Ni-Ni	0.86±0.07	2.50±0.06	7.9	7.0	0.011
	Ni-O	0.71±0.24	3.81±0.04	6.0	9.0	
Ni foil	Ni-Ni	12*	2.48±0.04	6.5	7.0	0.0039
NiO	Ni-Ni	12*	2.95±0.01	6.5	7.0	0.024
	Ni-O	6*	2.09±0.05	7.9	9.0	

^aCN: Coordination Number; ^bR: Atomic spacing; ^cσ²: Disorder factor; ^dΔE₀: Energy zero shift. The fitting of coordination number and bond length is subject to a certain range of errors influenced by experimental conditions, data processing methods, and structural model assumptions.

Supplementary Table 9. The fitting result of the XPS spectra of Ni 2p and Mo 3d in Ni@C-MoO_x and NiMoO_x.

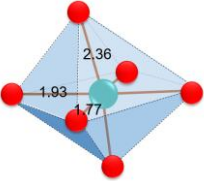
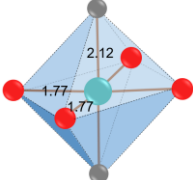
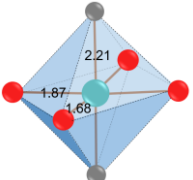
Sample	Species	Peak BE (eV)	FWHM (eV)	Atomic (%)
Ni@C-MoO _x	Ni ⁰	852.63	1.17	20.47
	Ni ^{σ+}	854.95	2.50	37.61
	Ni ²⁺	856.60	2.50	41.65
	Mo ⁴⁺	239.74	1.44	25.76
	Mo ⁵⁺	230.76	1.44	38.93
	Mo ⁶⁺	232.40	1.44	35.30
NiMoO _x	Ni ⁰	853.10	1.17	22.09
	Ni ^{σ+}	854.89	2.50	17.90
	Ni ²⁺	856.76	2.50	60.02
	Mo ⁴⁺	230.04	1.44	32.93
	Mo ⁵⁺	231.11	1.44	35.68
	Mo ⁶⁺	232.82	1.44	31.39

Supplementary Table 10. Structural parameters obtained from the curve-fitting analysis of the EXAFS spectra.

Sample (s0 = 0.85)	Bond	CN ^a	R(Å) ^b	σ^2 (10 ³ Å ²) ^c	ΔE_0 (eV) ^d	R factor
Ni@C-MoO_x	Mo-O	1.53±0.31	1.77±0.02	6.8	8.4	0.028
	Mo-C	1.82±0.24	2.12±0.01	1.2	3.1	
MoO₃	Mo-O	2*	1.77±0.01	6.8	6.5	0.024
	Mo-O	2*	1.93±0.03	1.7	6.5	
	Mo-O	1*	2.26±0.02	2.8	6.5	
	Mo-O	1*	2.36±0.02	3.9	6.5	
Mo	Mo-Mo	8*	2.73±0.01	3.2	-3.5	0.018
	Mo-Mo	6*	3.15±0.03	1.6	-3.8	

^aCN: Coordination Number; ^bR: Atomic spacing; ^c σ^2 : Disorder factor; ^d ΔE_0 : Energy zero shift. The fitting of coordination number and bond length is subject to a certain range of errors influenced by experimental conditions, data processing methods, and structural model assumptions.

Supplementary Table 11. The bond lengths in MoO₃ and C-MoO_x as determined by EXAFS and DFT calculation results.

Sample		Bond	Length (Å)
MoO₃		Mo-O1	1.77
		Mo-O2	1.93
		Mo-O3	2.36
C-MoO_x (EXAFS data)		Mo-O	1.77
		Mo-C	2.12
C-MoO_x (DFT data)		Mo-O1	1.68
		Mo-O2	1.87
		Mo-C	2.21

Supplementary Table 12. The Bader charge of atoms in Ni@C-MoO_x before and after one hydrogen (H) atom was adsorbed onto the Ni site.

Sites	Bulk (e)		Interface (e)	
	Before H	^b after H	Before H	^b after H
O-1	-1.00	-1.00	-0.96	-0.96
O-2	-0.86	-0.94	-0.98	-0.98
C-1	-0.92	-0.89	-0.73	-0.73
Mo-1	1.44	1.55	1.14	1.26
Mo-2	1.10	1.38	1.24	1.39
^aNi	-0.03	-0.03	0.19	0.20
^b Ni site with H	NA	NA	0.01	-0.03

^a The charge on Ni is the average of those Ni atoms with the same distance to interface.

^b Hydrogen adsorption on Ni site which was two-atom-distance away from the interface.

Supplementary Note 1

A linear σ coordination bond was formed between conjugated carbon (-C=C groups) and metal atoms during co-hydrolysis, as evidenced by the prominent features that emerged in the IR spectra and UV-vis absorption spectra after co-hydrolysis, including a more notable stretching vibration peak attributed to -C=C groups ($\sim 1630\text{ cm}^{-1}$) (Supplementary Fig. 2), a new p(carbon)-d(metal) electron transition absorption peak at 208 nm and a blueshift of the π (metal)- π^* (carbon) electron transition absorption peak (Supplementary Fig. 3)³. After subjecting the sample to H_2 reduction at 500 °C, the intensity of the p-d transition UV-vis peaks increased, and the -C=C stretching vibration peak in the IR spectrum remained, indicating the successful carbon doping into the final product of the Ni@C-MoO_x catalyst with carbon-metal coordination.

Supplementary Note 2

The exchange current density (j_0) calculated by the micro-polarization method for Ni@C-MoO_x coated on a rotating disk electrode was $0.92\text{ mA cm}^{-2}_{\text{disk}}$ at a Ni metal loading of 0.2 mg cm^{-2} , which was comparable to that of the Pt/C_{com} electrode ($1.41\text{ mA cm}^{-2}_{\text{disk}}$) (Supplementary Fig. 16, Supplementary Table 2). Note that the particle size of Pt was only one-tenth that of Ni, indicating that the intrinsic activity of the as-prepared Ni@C-MoO_x catalyst was comparable to that of Pt/C_{com} , and the activity was probably further enhanced by reducing the Ni particle size (Supplementary Table 3).

Supplementary Note 3

The conventional NiMoO_x catalyst prepared without carbon doping, another Ni@C-MoO_x catalyst produced by using tetraphenyl porphyrin instead of sodium chlorophyll-copper ($\text{Ni@C-MoO}_x\text{-TP}$), the Ni@C-MoO_x annealed in a N_2 atmosphere ($\text{Ni@C-MoO}_x\text{-N}_2$), the Ni/CuChl synthesized catalysts without Mo, and a commercial Pt/C catalyst (named Pt/C_{com}) were also evaluated for comparison. The Ni/CuChl and Ni@C-MoO_x without CuChl, however, showed no and low HOR currents compared to that of Ni@C-MoO_x , respectively (Supplementary Figs. 18 and 19). These results indicate that copper affected the active site formation, although copper was not present in the final catalyst; and Mo was crucial for active site formation. A similar electrooxidation resistance was observed for $\text{Ni@C-MoO}_x\text{-TP}$ and $\text{Ni@C-MoO}_x\text{-N}_2$ (Supplementary Figs. 19 and 20), indicating that carbon doping was the key for electro-oxidation resistance and that the doping of H during H_2 annealing for catalyst preparation was not necessary for the electrooxidation resistance.

Supplementary Note 4

The peak at approximately 864 eV was attributed to the Auger peak of F (KL2) (Supplementary Fig. 26), as Nafion resin was used as the binder for electrode preparation. To eliminate the influence of Nafion, the

QPCBP-10 ionomer was used as a binder to further evaluate the stabilities. As shown in Fig. 3e and Supplementary Table 5, the components of Ni⁰ in the Ni@C-MoO_x electrode decreased slightly from 16.38 atom% to 12.29 atom% after the step potential stability test. These results indicate a high anti-electrooxidation ability of the Ni@C-MoO_x catalyst, but the binder impacted the stability of the catalyst, which should be considered in fuel cell applications.

Supplementary Note 5

In-situ XRD and ex-situ TEM experiments were further performed to evaluate the stability of Ni@C-MoO_x. As shown in Supplementary Fig. 29, the metallic Ni(111) peak did not change at all with the potential applied, further indicating the good crystalline stability under such conditions. The ex-situ TEM images in Supplementary Fig. 30 also show no changes in the Ni nanoparticles of Ni@MoO_x after the stability test.

Supplementary Note 6

As shown in Supplementary Fig. 31, the hydrogen desorption behavior on Ni@C-MoO_x was very similar to that on Pt/C_{com}, with a desorption peak centered at ~350 °C and a shoulder peak at 270 °C, which corresponded to spillover hydrogen on the support and chemisorbed hydrogen on the metal surface, respectively⁴. The spillover hydrogen peak observed on the Ni@C-MoO_x and Pt/C_{com} catalysts was higher than that on NiMoO_x by ~70 °C, while the chemisorbed hydrogen peak was lower than that on NiMoO_x by less than 10 °C. These results indicate that the hydrogen bonding energy at the Ni site on Ni@C-MoO_x was only slightly reduced compared to that at the Ni site on NiMoO_x and was similar to that on Pt/C_{com}. The MoO_x and C-MoO_x supports, however, exhibited a chemical desorption peak of H₂ at approximately 408~381 °C, which is higher than that of Ni, suggesting that the sites on MoO_x and C-MoO_x may adsorb hydrogen too strongly compared to those on Ni, and therefore may not be the most active ones for catalyzing the HOR (Supplementary Fig. 31). These results agreed with the DFT calculations. As shown in Supplementary Figs. 32 and 33, the hydrogen adsorption free energies (ΔG_H) on all Ni sites exhibited the closest values to that on Pt, among all these typical 16 sites, such as Mo sites and C sites, on Ni (111), NiMoO_x and Ni@C-MoO_x models. Further calculations of ΔG_H at different H₂ coverages showed that the hydrogen binding energy (HBE) of Ni-fcc for NiMoO_x and Ni@C-MoO_x increases with increasing H₂ coverage on the Ni surface, and that the HBE of Ni@C-MoO_x is slightly higher than that of NiMoO_x (Supplementary Fig. 33). This is consistent with the slightly higher HOR performance of NiMoO_x (Supplementary Figs. 16 and 34). The interfacial Ni sites near to C-MoO_x are more appropriate for the HOR than Ni sites away from the interface, which showed a ΔG_H of -0.033 eV that is even more desirable than that on Pt sites. This result indicates that the Ni sites are active for the HOR and that the constructed interface would enhance the activity of Ni sites. Further evidence was found in controlled synthesis and the etching

experiments. As shown in Supplementary Fig. 35, no HOR current was detected for Ni@C-MoO_x catalyst that had been reduced at 300 °C due to no metallic Ni being produced. This is in strong contrast to the case of Ni@C-MoO_x catalyst that had been reduced at 500 °C where metallic Ni formed, which exhibited a high HOR activity under the same conditions. In addition, the Ni@C-MoO_x catalyst lost approximately half its activity for the HOR after 15 acidic etching cycles in a 0.1 M HClO₄ solution (Supplementary Fig. 36). Correspondingly, approximately 40% of the Ni was lost in the etching process (Supplementary Table 6). Furthermore, it was noted that the NiMoO_x catalyst lost all its activity for HOR after the same etching process where almost no Ni remained. Surprisingly, we found that the developed Ni@C-MoO_x catalyzed the HOR even in an acidic medium (Supplementary Fig. 37) with a steady output HOR current for more than 10 hours, indicating that the combination of metallic Ni and the C-MoO_x layer protected Ni from acidic etching, leading to a stable site for acidic HOR catalysis as well as for the alkaline HOR.

Supplementary Note 7

The R-space of the Ni of Ni@C-MoO_x was also very similar to those of the traditional NiMoO_x catalyst and Ni foil (Supplementary Figs. 40 and 41 and Supplementary Table 8). These results indicated that the coordination environment of the Ni in Ni@C-MoO_x was not significantly changed compared to that of Ni metal, which is different from previously reported Ni catalysts. These results are consistent with the observation that Ni@C-MoO_x and NiMoO_x exhibited a similar exchange current density. However, a notable negative chemical shift was observed in the Ni 2p XPS spectrum of Ni@C-MoO_x compared to that of NiMoO_x (Supplementary Fig. 42 and Supplementary Table 9) on the surface. Therefore, the influence of free electrons on the electronic structure of Ni cannot be ruled out ⁵.

Supplementary Note 8

The pre-peak at ~20005 eV was observed for MoO₃ but absent for MoO₂ (Fig. 5b), indicating that the O-Mo-O octahedron coordination structure existing in MoO₂ became distorted with the asymmetric O-Mo-O octahedron coordination structure in MoO₃ ⁶.

Supplementary Note 9

As shown in Fig. 5d the broadened peak at reduced distance of 1~2 Å was fitted as one main peak at 1.6 Å plus a tail peak at 1.85 Å, corresponding to Mo-O and Mo-C bonds, respectively. The wavelet transforms of the Mo k-edge EXAFS, as shown in Supplementary Fig. 43, further evidenced the co-existence of Mo-O and Mo-C coordination in Ni@C-MoO_x powder. Two relatively high-intensity regions were observed at 1.6 Å and 1.85 Å for Ni@C-MoO_x, and they were assigned to Mo-C and Mo-O coordination, respectively. As shown in Supplementary Table 10, the fitted lengths for the Mo-O bonds were 1.77 Å and 2.12 Å in Ni@C-

MoO_x, which were consistent with the simulation results in Supplementary Fig. 41 and Supplementary Table 11 (1.68 Å and 2.24 Å). Note that the Mo-O bond in Ni@C-MoO_x was obviously shortened after carbon doping, and the newly formed Mo-C bond was longer than the original Mo-O bond in MoO₃ (Supplementary Fig. 43).

Supplementary Note 10

The Bader analysis is numerically difficult as there are many factors that can affect the analysis. From this, we further calculated the differential charge density of the interface atoms for Ni@C-MoO_x and NiMoO_x after hydrogen adsorption. Therefore, the changed charge density can only be ascribed to the adsorption of hydrogen. As shown in Supplementary Fig. 50, significant electron loss was observed on the Mo atoms of Ni@C-MoO_x at the interface after hydrogen adsorption on the Ni atoms. In contrast, for the Mo of NiMoO_x under the same conditions, almost no change was observed. We further synthesized the Ni@C-MoO_x catalysts at different degrees of confinement by increasing or decreasing the addition of carbon precursor. As shown in Supplementary Fig. 51, increasing carbon doping enhanced the protection against Ni electrooxidation but led to a weakened HOR performance. Decreasing the carbon addition, however, weakened the quantum confinement leading to an enhanced HOR performance and a weakened protection against Ni electrooxidation. Further investigations with in-situ XAS experiments were performed. As shown in Supplementary Fig. 52, the NiMoO_x modified electrodes show a significant positive shift of 0.18 eV in the k-edge of Ni during the HOR catalysis at 0.1 V compared to the original one. The positive shift of the k-edge indicates that Ni lost electrons and was oxidized during HOR catalysis. This is in strong contrast to the Ni@C-MoO_x catalyst, whose k-edge remained or even slightly shifted negatively under HOR catalysis at 0.1 V. The small negative shift indicates the electron gained at such an anodic potential.

Supplementary Note 11

The similarities and differences between the quantum well catalytic structure (QWCS) and quantum well (QW) from the traditional physics perspectives.

(i) Structural similarity

QW (three-layer-structure): The simplest quantum well system is constructed by insetting a thin layer of one type of semiconductor material between the layers of another with different band gap to form a three-layer-structure.

QWCS (five-layer-structure): The slice based on the electron pathway, as shown in Supplementary Fig. 1, simplified the QWCS into a five-layer structure. That is, a Ni metal layer is sandwiched between two C-MoO_x layers (acceptor-doped n-type semiconductor), which is further sandwiched by two n-type MoO_x layers.

(ii) Property similarity

QW: QW allows charge carriers to be confined in well-defined regions and provides energy conversion to light at desired wavelengths. The widest application of QW, transistor, is used in a circuit to control a large amount of current or voltage with a small amount of voltage or current. This means that it can be used to amplify or switch (rectify) electrical signals or power.

QWCS: QWCS allows electrons to be confined or traversed in well-defined regions based on the adsorption on the QWCS. That is, the conductivity of C-MoO_x (well) is activated by hydrogen adsorption but shielded by the oxygen-contained species adsorption (Supplementary Fig. 2). This means that it can be used to switch reactions when electrochemical oxidation occurs.

The role of each component and the catalytic behavior can be summarized as follows:

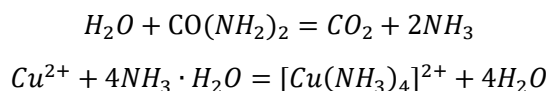
Ni was evidenced as the major active site for HOR. H₂ molecules and OH⁻ species in the electrolyte could penetrate through defects or pores (around 0.5 to 1 nm) on C-MoO_x thin layer (about 1 nm) to reach Ni sites for reaction. The Ni nanoparticles and C-MoO_x layer shared the same electron pathway whose electronic conductivity depends on the adsorption on the Ni sites and/or C-MoO_x layer, which locks or unlocks for the further catalytic process. DFT calculations show that an exciton-like combination was produced at the interface between Ni and Mo (electron state at Mo and hole state at Ni), which confined the electrons within the interface. There were approximately 0.3 e⁻ negative charges being transferred into Mo, where one third of them were from Ni. The negative charges on Mo reduced when hydrogen adsorbed onto the Ni site. This indicates the exciton-like combination vanished with hydrogen adsorption, allowing the transfer of electrons, and leading to the catalytic gating property. This is like the quantum confinement effect. Such phenomenon cannot be observed between the Ni and MoO_x layer.

Supplementary Note 12

As shown in Supplementary Fig. 8, many defects and nano-pores were present on the C-MoO_x thin layer with 1 nm thickness. The sizes of the defects and nano-pores were around 0.5 to 1 nm which are large enough for the penetration of H₂ (0.289 nm), OH⁻ ion (0.137 nm) and H₂O (~0.4 nm). Moreover, a gentle acidic etching experiment by cycling in a 0.1 M HClO₄ solution demonstrated an obvious Ni mass loss and activity decline (Supplementary Fig. 33) for Ni@C-MoO_x, providing further evidence for the fact that the electrolyte and hydrogen could pass through the defects and nano-pores of the outer C-MoO_x thin layer and reach the confined Ni site.

Supplementary Note 13

Sodium copper chlorophyllin was introduced as carbon doping precursor to construct quantum wells around the Ni nanoparticles, because of its strong coordination with Mo atoms. However, the copper would coordinate with ammonia to form complex ions which then dissolved in water at temperature of 160 °C.



As shown in Supplementary Fig. 17a, the solution showed the specific blue color of Cu^{2+} after hydrothermal reaction, indicating that Cu^{2+} was dissolved with ammonia during hydrothermal process. And no characteristic peak was detected for copper in XPS (~930 eV) as shown in Supplementary Fig. 17b. The replacement of Cu-chlorophyllin coordination by Mo-chlorophyllin in the existence of $(NH_2)_2CO$ solution is curial for the catalyst preparation with high activity.

We further replaced the sodium chlorophyll-copper by tetraphenyl porphyrin to synthesis the catalyst. As shown in Supplementary Figs. 17c and d, the catalyst produced without Cu exhibited a relatively low activity for HOR but a similar anti-oxidation resistance during the catalysis. These results indicate that the copper did affect the formation of active sites but did not participate in the catalysis as a component.

Supplementary Note 14

Density functional theory (DFT) calculation was used to screen the active sites of the produced catalyst. The hydrogen adsorption free energy (ΔG_H) on Ni was used as a descriptor of HOR catalytic activity⁷. Three catalytic models, i.e., Ni(111), NiMoO_x and Ni@C-MoO_x, were constructed; and typical 16 sites were selected for the investigation. The ΔG_H on Pt was also calculated as a benchmark for comparison. As shown in Supplementary Fig. 32, the ΔG_H on all Ni sites exhibited the closest values to that on Pt, among all these typical 16 sites. The Mo sites and C sites, however, showed a relatively higher ΔG_H over Ni for HOR. In addition, the interfacial Ni sites near to C-MoO_x or MoO_x are more appropriate for the HOR than Ni sites away from the interface. The ΔG_H (-0.033 eV) is even more desirable than that on Pt site. This result indicates that the Ni sites are active for HOR and that the constructed interface would enhance the activity of Ni sites.

Supplementary Note 15

To investigate how hydrogen adsorption on Ni would impact the nature of C-MoO_x out layer in the Ni@C-MoO_x, we further calculated the charge of the C-MoO_x before and after hydrogen was adsorbed onto Ni atoms. Two typical Mo atoms at the interface between Ni and C-MoO_x were selected for observation. As shown in Supplementary Fig. 47, the charge dramatically increased by about 10% in Mo atoms after only one hydrogen atom adsorbed onto Ni site of Ni@C-MoO_x. In contrast, only a tiny change by ~2% in Mo was observed from NiMoO_x. This result indicates an obvious electron transfer between Ni and C-MoO_x occurred upon H₂ adsorption on Ni. It is interesting that an obvious loss of electrons was clearly observed

for all the Mo atoms (whatever they are near to or away from the interface) even when just one hydrogen atom was adsorbed onto the Ni site that is two-atom-distance away from the interface (as shown in Supplementary Fig. 47 and Supplementary Table 11). The Ni site with H adsorption, as well as the nearby atoms, however, showed almost no change in charge at all (Supplementary Table 11). These results indicate that the adsorbed hydrogen on Ni can greatly influence the charge of Mo which is far away from the H-adsorbed Ni site. In another word, the interfacial dipole effect (electron at Mo and hole at Ni) vanished upon hydrogen adsorption and eventually led to relieving the confinement for charge-transfer in gate operation (Fig. 6).

Supplementary Note 16

Interfacial dipole effect: The typical feature is that the produced excitons which are the combinations of electron and hole, are free to move as a unit but confined in all three spatial dimensions. Thus, we prefer to name the catalyst as “quantum-confinement-induced electrocatalyst”, due to the quantum confinement mechanism for gating operation. In the Ni@C-MoO_x catalyst, an exciton-like combination was produced at the interface between Ni and Mo (electron state at Mo and hole state at Ni), which confined the electrons within the interface. In addition, an obvious loss of electrons occurred on all the Mo atoms (whatever they are near to or away from the interface) even when just one hydrogen atom was adsorbed onto the Ni site that is two-atom-distance away from the interface (as shown in Supplementary Fig. 48 and Supplementary Table 12). This indicates the interfacial dipole effect vanished with hydrogen atom adsorbed on Ni site for gating operation. To distinguish it from the physical term exciton, we refer to this phenomenon as the “*interfacial dipole effect*”.

Supplementary References

- 1 Wei, C., Reshma, R., Peng, J., Huang, B. *et al.* Recommended Practices and Benchmark Activity for Hydrogen and Oxygen Electrocatalysis in Water Splitting and Fuel Cells. *Adv. Mater.* **31**, 1806296 (2019).
- 2 Lu, S. & Zhuang, Z. Investigating the influences of the adsorbed species on catalytic activity for hydrogen oxidation reaction in alkaline electrolyte. *J. Am. Chem. Soc.* **139**, 5156–5163 (2017).
- 3 Xu, W., Zhang, T., Bai, R., Zhang, P. & Yu, J. A one-step rapid synthesis of TS-1 zeolites with highly catalytically active mononuclear TiO₆ species. *J. Mater. Chem. A* **8**, 9677-9683 (2020).
- 4 Miller J. T. *et al.* Hydrogen temperature-programmed desorption (H₂ TPD) of supported platinum catalysts. *J. Catal.* **143**, 395-408 (1993).
- 5 Gao, F.-Y. *et al.* Gao, FY., Liu, SN., Ge, JC. *et al.* Nickel–molybdenum–niobium metallic glass for efficient hydrogen oxidation in hydroxide exchange membrane fuel cells. *Nat. Catal.* **5**, 993–1005 (2022).
- 6 Zheng, Y. *et al.* Molybdenum Oxide, Oxycarbide, and Carbide: Controlling the Dynamic Composition, Size, and Catalytic Activity of Zeolite-Supported Nanostructures. *J. Phys. Chem. C* **123**, 22281-22292 (2019).
- 7 Nørskov, J. K. *et al.* Trends in the Exchange Current for Hydrogen Evolution. *J. Electrochem. Soc.* **152**, J23 (2005).